Article:
Olivucci, P., Ricco, P. orcid.org/0000-0003-1537-1667 and Aghdam, S.K. (2019) Turbulent drag reduction by rotating rings and wall-distributed actuation. Physical Review Fluids, 4 (9).

https://doi.org/10.1103/physrevfluids.4.093904

Turbulent drag reduction by rotating rings and wall-distributed actuation

Paolo Olivucci, Pierre Ricco, and Sohrab Khosh Aghdam
Department of Mechanical Engineering, University of Sheffield, Sheffield S1 4DE, United Kingdom

September 22, 2019

Abstract

Olivucci, P. Ricco, P. Aghdam, S.K. "Turbulent drag reduction by rotating rings and wall-distributed actuation", Phys. Rev. Fluids, 4, 093904.

Turbulent channel flows altered by the combination of flush-mounted spinning rings and vertical-velocity opposition control or hydrophobic surfaces are studied through direct numerical simulations. The two types of distributed control are applied over the surface area that is not occupied by the spinning rings. The turbulent mean skin friction is reduced by 20% through the steady rotation of the rings and the effect is enhanced by the distributed controls, reaching a drag reduction of 27%. The numerically-computed combined drag reduction is well predicted by an upper bound obtained by a simple idealized model. The turbulence statistics are highly non-uniform along the spanwise direction, but show a weak dependence along the streamwise direction. The wall-shear stress is highly reduced over the central region of the rings. Narrow streamwise-elongated structures forming between adjacent discs offer a detrimental global contribution to the Reynolds stresses, although locally they reduce drag. A spatially-dependent form of the Fukagata-Iwamoto-Kasagi identity helps explain the different influence of the two distributed controls, although the global drag reduction levels are similar. The opposition control is effective in altering the elongated structures between rings, but it does not contribute to enhance the drag reduction in the central ring region. Hydrophobicity creates a more non-uniform flow and even enhances the intensity of the streamwise structures between rings, but further reduces the wall-shear stress in the central ring region compared to the rings-only case. The mean wall-slip velocity is the additional beneficial effect offered by the hydrophobic surface between rings.

Introduction

Turbulent skin-friction drag reduction has been the subject of great interest in fluid mechanics research for its potential advantages to limiting fuel consumption in the airline and marine transport industries and to tackling the pressing problem of environmental pollution. Flow control techniques aimed at drag reduction can be classified as active

or passive. Active methods are those requiring an external energy input to manipulate the flow, while passive methods do not necessitate such an input as the flow changes are usually achieved via geometrical modifications of the surface.

The purpose of a wall-based drag reduction technique is to disrupt the self-sustaining process of near-wall turbulence and to attenuate the bursts that promote the turbulent transport of near-wall high-momentum fluid, which leads to high skin friction. At the low Reynolds number considered in this study, the near-wall dynamics is responsible for most of the friction at the wall (Quadrio, 2011).

Drag reduction by in-plane wall motion was originally introduced by Jung et al. (1992), who demonstrated the possibility of decreasing the turbulent skin friction by oscillating the wall in the cross-flow direction. Steady and traveling waves of spanwise velocity at the wall were also shown to lead to drag reductions as high as 45% (Quadrio et al., 2009). Several researchers have investigated the mechanism by which the spanwise wall motion acts on the near-wall turbulence to suppress the turbulent activity, leading to drag reduction (Choi, 2002; Quadrio, 2011; Skote, 2011; Ricco et al., 2012; Duque-Daza et al., 2012; Blesbois et al., 2013; Lardeau and Leschziner, 2013). Quadrio and Ricco (2004) remarked that the forcing period $T^+ = 100$ (where the superscript $+$ denotes scaling in viscous units) causes maximum drag reduction because it matches a characteristic temporal scale of the near-wall turbulent structures. This forcing period also corresponds to an optimal thickness of the spanwise Stokes layer. This optimal Stokes layer directly affects the buffer-layer velocity streaks, as it is a few wall-units thick. The visualizations by Ricco (2004) distinctly show that the streaks are dragged laterally by the spanwise shear of the Stokes layer, while the shorter, faster-traveling quasi-streamwise vortices located above the streaks (Adrian, 2007) and above the Stokes layer do not move laterally, but are only indirectly altered by the wall forcing as their energy is attenuated. Further evidence of the scaling of the drag reduction with the viscous penetration length has been reported by Quadrio and Ricco (2011) for the case of the generalized Airy-function Stokes layer produced by the streamwise-traveling spanwise-velocity waves. A minimal forcing amplitude has been found, i.e., the maximum velocity of the wall must be larger than a minimal value to affect the near-wall turbulence and cause drag reduction.

Flush-mounted spinning discs have also been proved to be a promising technique for turbulent drag reduction, yielding up to around 23% drag reduction at low Reynolds numbers (Ricco and Hahn, 2013; Wise and Ricco, 2014; Wise et al., 2014). Wise et al. (2014) showed that annular actuators, or "rings", with an optimal inner-to-outer radius ratio equal to 0.6 deliver a slightly larger drag reduction than the full discs, while requiring up to 20% less driving power. The rings used by Wise et al. (2014) covered 50% of the wall area, while the other half of the surface was stationary. Although the rings generate a maximum drag reduction of about 20%, thus smaller than the uniform spanwise-wall oscillations, the net power saved, computed by accounting for the frictional resistance of the fluid, is comparable for the two methods, about 10%. Advantages of the rings with respect to the in-plane motions are the localized actuation, the double optimal spanwise forcing scale, and the wide range of diameters leading to drag reductions that

are comparable with the maximum (Ricco and Hahn, 2013; Wise et al., 2014).

In the present paper we study the spinning rings in detail and we utilize the stationary wall surface confined between the rings and within the circles defining the inner-ring edges to enhance the drag-reduction performance by enforcing two types of distributed control. The word "distributed" is used herein to indicate that the control scale matches that of the near-wall turbulence, acting locally on the turbulent structures. This implies that the control performance is expected to scale proportionally to the actuated area. The two distributed control methods considered in this work are opposition control and hydrophobic surfaces.

Opposition control (OC) is an active control technique (Choi et al., 1994; Hammond et al., 1998) that works by detecting the instantaneous wall-normal velocity on a wall-parallel plane located at a height of y_d and, at the same time, by forcing the wall-normal wall velocity by the same amount of that detected in the y_d-plane, but with opposite sign:

$$v(x, 0, z, t) = -v(x, y_d, z, t). \tag{1.1}$$

This may result in drag reduction as a consequence of the attenuation of the sweeping motions of high-momentum fluid toward the wall and of the ejections from the near-wall region towards the bulk of the flow. The detection plane acts as a virtual wall, which means that any convective transport of momentum between the plane and the physical wall is greatly hampered. The optimal distance of the detection plane is $y_d^+ \approx 15$ (Choi et al., 1994). This flow has been further examined by Chung and Talha (2011), who considered several detection planes and wall-forcing amplitudes. The dependence of drag reduction on the wall-normal location of the detection plane is linked to the relative position of this plane with respect to the near-wall eddies. If the plane is placed underneath the quasi-streamwise vortices, the OC actuation has a beneficial effect due to the disruption of the near-wall ejections and sweeps. If instead the plane is too distant from the wall, the OC actuation promotes the momentum transport and the drag increases. In our study the location of the detection plane has been fixed to $y^+ = 14.5$, scaled in terms of the wall units of the reference fixed-wall channel.

The drag reduction effect produced by the hydrophobic surfaces (HS) has been explained in terms of the shift of the virtual origin of the mean velocity profile (Min and Kim, 2004). The slip length that models the hydrophobic surface allows the streamwise velocity to take a finite value at the wall, which means that the point where the extrapolated velocity vanishes (the virtual origin) is shifted below the wall surface. This attenuates the intense sweeps and ejections typical of the no-slip wall layer. A spanwise wall slip instead promotes the growth of streamwise rolls leading to drag increase due to an enhanced lift-up effect. Both constant (Min and Kim, 2004) and shear-dependent (Aghdam and Ricco, 2016) slip-length wall boundary conditions have been proposed to describe the effect of different types of hydrophobic surfaces, modeling lotus-leaf-type surfaces, where air pockets are trapped in small cavities (Ling et al., 2017; Seo et al., 2018; Reholon and Ghaemi, 2018), and pitcher-plant-type surfaces, where oil is imbibed in the porous surface (Wong et al., 2011) or in transverse microcavities (Ge et al., 2018). In the present work we follow the approach of Min and Kim (2004) where the no-slip

boundary condition on the streamwise velocity is replaced by the following constant-slip-length condition:

$$u(x, 0, z, t) = l_s \left. \frac{\partial u}{\partial y} \right|_{y=0}. \tag{1.2}$$

Objectives

The objectives of the present work are

- to further the understanding of physical mechanisms behind the drag-reduction effects induced by the spinning discs. In particular, we are interested in studying the streamwise-elongated structures appearing between spanwise-adjacent discs that have been reported by Ricco and Hahn (2013), Wise and Ricco (2014), and Wise et al. (2014) to contribute significantly to the alteration of the near-wall momentum exchange;

- to enhance the drag-reduction performance given by the spinning rings by enforcing two different types of distributed control, i.e., opposition control based on wall-normal velocity actuation and hydrophobic surfaces. We aim to maintain the localized rotation that Ricco and Hahn (2013), Wise and Ricco (2014), and Wise et al. (2014) have shown to be effective in operating at large-flow scales and, at the same time, we want to evince whether the distributed control methods can weaken the elongated structures between rings that contribute detrimentally to drag reduction Wise et al. (2018). The original publications by Keefe (1997, 1998) do suggest to utilize the space between and within the rotating actuators to enforce wall-normal transpiration to fully specify a three-dimensional flow field. Keefe (1998) states:"Suction and blowing holes can be interspersed among, or made coaxial with, the disks for creating general three-dimensional velocity perturbations in the near-surface region." Figure 1 shows an adaptation of the original sketch by Keefe (1998) where the flow is actuated by rotating discs and wall transpiration. To the best of our knowledge, active three-dimensional flow control techniques are not investigated at present;

- for the first time, to develop and use an extended form of the Fukagata-Iwamoto-Kasagi identity (Fukagata et al., 2002) that can be employed to study active control strategies that are non-uniform in both the streamwise and spanwise directions.

- to advance a simple idealized model for predicting the upper bound of the drag reduction that can be achieved by combining the spinning-ring method and the distributed control actuations. This approach can be easily generalized to other combinations of drag-reduction techniques.

Section 2 describes the solver of the Navier-Stokes equations, the numerical procedures, the statistical tools, and the decomposition of the flow variables. Section 3 discusses the flow visualizations, the turbulence statistics, and the turbulent drag reduction. A summary of the results is presented in §4.

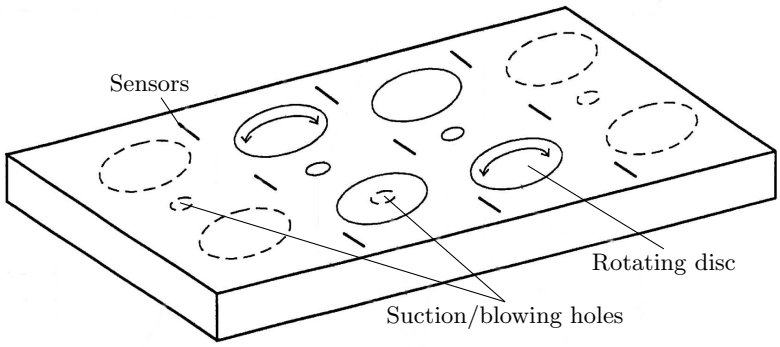

Figure 1: Schematic of rotating discs actuators, combined with wall transpiration, adapted from the original sketch of Keefe (1998).

Numerical and statistical procedures

Numerical simulations

The combined effect of the spinning rings and the distributed forcing on wall turbulence is tested numerically in a channel with periodic boundary conditions along the streamwise direction x^* and the spanwise direction z^*. Dimensional quantities are henceforth denoted by the superscript $*$. The wall-normal coordinate is y^* and the parallel walls are separated by a distance $2h^*$. The numerical domain of the channel has dimensions L_x^* and L_z^* along x^* and z^*, respectively, and the velocity components are u^*, v^*, and w^* along x^*, y^*, and z^*, respectively. A ring is characterized by the outer diameter D^* and the inner diameter D_i^*. The shape factor $a = D_i^*/D^*$ is fixed for all the cases at the optimal value of 0.6 found by Wise et al. (2014). The portion of the wall surface that is not covered by the rings is subjected to the distributed actuation. For $a = 0.6$ this part of the surface amounts to 50% of the total wall surface. The ring motion is defined by the constant velocity W^* at the outer edge. Each ring has two $0.05D^*$-wide gaps along the internal and external edges, where the velocity decays from the edge values to zero, following a linear profile. This greatly reduces the numerical oscillations arising from the sharp velocity discontinuity that would occur if the gaps were not present (Ricco and Hahn, 2013) and also models the absence of rigid wall between the rings and the stationary surface that would unavoidably occur in a laboratory set-up. Extensive resolution checks have been carried out to ensure the robustness and accuracy of the drag reduction values and of the turbulent statistics. The rings are fitted on both walls and form spanwise rows spanning the entire channel width, as shown in Fig. 2. Rings belonging to the same row share the same sense of rotation, which is opposite to that of the next row. This arrangement creates triangular waves of spanwise velocity along the streamwise lines passing through the centers of the rings, thereby resembling the standing wall waves that have been shown to be very effective in reducing the turbulent

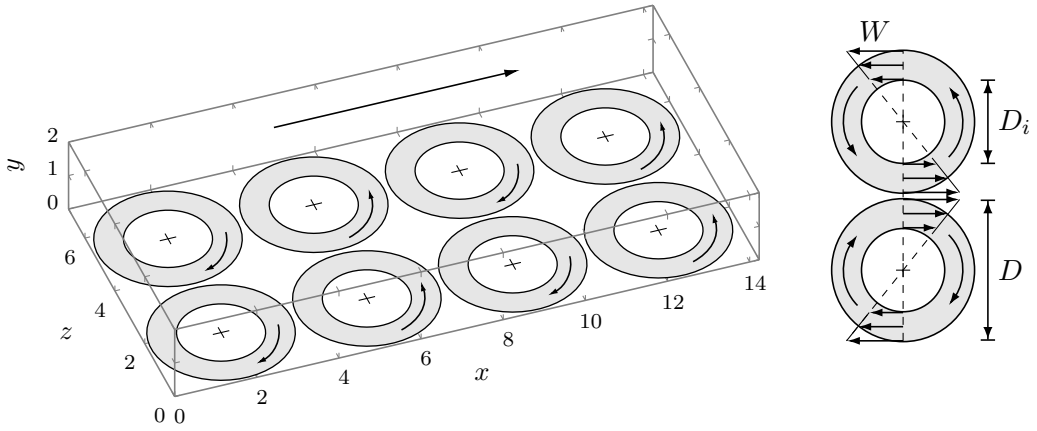

Figure 2: Schematic of the arrangement of the ring-fitted channel. Only the rings on the bottom wall are shown. The rings are shown in grey, while distributed actuation is applied in the white regions. The sense of rotation of the rings is highlighted by the curved arrows, while the longer arrow indicates the mean-flow direction. The sketch on the right illustrates the triangular-wave spanwise velocity pattern created along the centerline of the rings by two streamwise-adjacent counter-rotating rings.

drag (Quadrio et al., 2009).

The flow is simulated using the code Incompact3D (Laizet and Li, 2011; Laizet and Lamballais, 2009), run on the Cray XC30 "Archer" supercomputer of the National Supercomputing Service. The code integrates the non-dimensional incompressible Navier-Stokes equations using a Chorin-Temam projection method, with the time advancement performed by a second-order Adams-Bashforth scheme. The spatial discretization of the momentum equations is obtained by compact finite difference schemes of maximum order equal to six in the interior of the domain. The Poisson equation for the projection pressure is solved in spectral space using a fast Fourier transform on a partially staggered grid. The grid is uniformly spaced along x and z. Along y, the grid is stretched as the points are clustered more compactly near the walls to ensure that the near-wall small scales are accurately resolved. Incompact3D adopts the Message Passing Interface parallelism and exhibits excellent scalability, achieved by implementing a 2D domain decomposition (Laizet and Li, 2011). The simulations are run using 1024 parallel computational cores and adopting a 32×32 block decomposition.

Quantities scaled in outer units, i.e., by the channel half-height h^* and the centerline velocity U_p^* of the laminar parabolic Poiseuille flow at the same flow rate, are not indicated by any symbol. The diameter and the tip outer velocity of the rings are kept constant to $D = 3.39$ and $W = 0.38$ to focus on the combined effect of the spinning rings and the distributed control. This pair of W and D leads to the near-optimum drag reduction of 19.5% for the full discs (Ricco and Hahn, 2013) which increases to 20% for the rings with $a = 0.6$. Scaled in the wall units of the reference channel, these parameters are $W^+ = 9$ and $D^+ = 604$. The fluid flows at the fixed volumetric flow

rate per unit spanwise depth of $2h^*U_p^*/3$ in all the cases. This is maintained by applying a numerical correction to the mean velocity profile at every time step. The Poiseuille Reynolds number is $Re_p = U_p^* h^*/\nu^* = 4200$, where ν^* is the kinematic viscosity of the fluid.

The computations are initiated from the laminar Poiseuille channel flow between solid stationary walls, disturbed by random velocity fluctuations. This initial flow field evolves to the fully-developed uncontrolled turbulent flow, identified by the main statistics displaying convergence and the total mean stress profile being linear (Orlandi, 2012). This reference fully-developed turbulent flow is used as the initial flow for the computations of the controlled cases. The initial transient flow response to the modified boundary conditions is discarded to acquire meaningful statistics of the controlled flow. The flow statistics are collected by averaging well-delayed velocity and pressure flow fields at a temporal distance of about $t_d^+ = 20$ to reduce the statistical correlation between the flow fields. The total averaging time is $t_a = 950$, starting from the end of the transient flow.

Table 1 summarizes the main numerical parameters of the simulations. The wall no-slip Dirichlet boundary condition is used to impose the ring motion and the wall-transpiration boundary condition (1.1) is enforced for the OC simulations. When OC is applied to the entire wall surface through condition (1.1), the suction/blowing mean flow rate at the walls is zero, but in the combined ROC case a mean negative wall velocity $V_{oc}(y = 0)$ of the order of 10^{-4} exists if (1.1) is applied over the portion of the wall not covered by the rings. Above this controlled-wall region in the plane $y = y_d$ the wall-normal velocity has a positive mean value, which is mainly due to the wall-normal ejections associated with the streamwise-elongated structures existing between rings. It is clear from the continuity equation that, in order to maintain a constant mass flow rate at each streamwise location and at each time step, it is therefore not sufficient to impose (1.1) only, but it is also necessary to impose a blowing wall velocity $-V_{oc}(y = 0)$ over the surface not occupied by the rings to obtain $V = 0$ at the wall and at any wall-normal location. The Robin boundary condition at the wall (1.2) is applied to simulate the HS. We take the slip length to be $l_s = l_s^*/h^* = 0.02$, yielding a drag reduction of about 30% (Min and Kim, 2004) at low Reynolds numbers. This slip length corresponds to a realistic physical value $l_s^* = 100\mu$m for a channel height of about 1 cm (Lauga and Stone, 2003; Choi and Kim, 2006; Bidkar et al., 2014).

In table 1 and henceforth, the letter "R" indicates ring forcing, while "OC" and "HS" refer to the cases where the distributed control is applied on the entire wall surface. "R0" denotes cases where the rings do not move and the distributed control is applied over the portion of the surface that is not covered by the rings. The letters "ROC" and "RHS" denote the combined cases of rings with opposition control and rings with hydrophobic wall, respectively. These notations are also used as subscripts to indicate that a quantity refers to that specific case.

Averaging operators

In this section the averaging operators are defined. The time average of a flow variable $f(x, y, z, t)$ over a time interval $[0, T]$ for which f is statistically stationary is defined as:

Table 1: Simulation parameters. The ring outer diameter D^+ and tip velocity W^+ are scaled in the wall units of the reference channel flow. The number of grid points are along x, y, and z, respectively. The Reynolds number is $Re_p = 4200$ and the inner-outer diameter ratio is $a = 0.6$ for all the cases.

Case	$L_x \times L_z$	grid points	D^+	W^+
Reference flow	$4\pi\times1.33\pi$	256×129×128	-	-
Opposition control (OC)	$4\pi\times1.33\pi$	256×129×128	-	-
Hydrophobic surface (HS)	$4\pi\times1.33\pi$	256×129×128	-	-
Rings (R)	$4.53\pi\times2.26\pi$	256×129×256	605	9
Rings + oppos. control (ROC)	$4.53\pi\times2.26\pi$	256×129×256	605	9
Rings + hydroph. surface (RHS)	$4.53\pi\times2.26\pi$	256×129×256	605	9
Hydroph. surface + fixed rings (HSR0)	$4.53\pi\times2.26\pi$	256×129×256	605	0
Oppos. control + fixed rings (OCR0)	$4.53\pi\times2.26\pi$	256×129×256	605	0

Time average

$$\overline{f}(x,y,z) = \frac{1}{T}\int_0^T f(x,y,z,t)\,\mathrm{d}t. \tag{2.1}$$

The flow is statistically periodic along x with period $2D$ and along z with period D, that is, the minimal geometrical flow unit that repeats itself along the streamwise and spanwise directions consists of two streamwise-adjacent rings spinning in opposite directions. A spatial ensemble-averaging operator is therefore defined as:

Spatial ensemble average

$$[f]_e(x_e,y,z_e,t) = \frac{2}{N_xN_z}\sum_{n_x=0}^{N_x/2-1}\sum_{n_z=0}^{N_z-1} f\left(x+2n_xD, y, z+n_zD, t\right), \tag{2.2}$$

where $0 \le x_e \le 2D$ and $0 \le z_e \le D$ are the ensemble spatial coordinates, while N_x and N_z are the number of rings in the numerical domain along x and z, respectively. The two streamwise-adjacent rings share a statistical mirror symmetry, which allows us to symmetry-average the ensemble-averaged flow quantities as follows:

Two-disc symmetry average

$$[u]_s(x_s,y,z_s,t) = \left\{[u]_e(x_e,y,z_e,t) + [u]_e(x_e+D,y,-z_e,t)\right\}/2, \tag{2.3}$$
$$[v]_s(x_s,y,z_s,t) = \left\{[v]_e(x_e,y,z_e,t) + [v]_e(x_e+D,y,-z_e,t)\right\}/2, \tag{2.4}$$
$$[w]_s(x_s,y,z_s,t) = \left\{[w]_e(x_e,y,z_e,t) - [w]_e(x_e+D,y,-z_e,t)\right\}/2, \tag{2.5}$$
$$[p]_s(x_s,y,z_s,t) = \left\{[p]_e(x_e,y,z_e,t) + [p]_e(x_e+D,y,-z_e,t)\right\}/2, \tag{2.6}$$

where $-D/2 \le x_s, z_s \le D/2$ and $\{x_e, z_e\} = \{0, 0\}$ is at center of one ring. We choose to maintain the spatial ensemble average (2.2) and the two-disc symmetry average (2.3) separate for clarity of notation and because flow visualizations in Fig. (a) utilize the x_e, z_e coordinates.

Spatial averaging along x_s and z_s, i.e., averaging over wall-parallel planes and over a square of size D^2 confining the minimal symmetry-averaged flow unit generated by one spinning ring, is defined as:

Spatial average

$$\langle f \rangle(y,t) = \frac{1}{D^2} \int_{-D/2}^{D/2} \int_{-D/2}^{D/2} [f]_s (x_s, y, z_s, t) \, \mathrm{d}x_s \mathrm{d}z_s. \tag{2.7}$$

The statistical sample is doubled by averaging a quantity across the two channel halves. A capital letter indicates a global average, $F(y) = [f]_g$, defined as:

Global average

$$[f]_g = \langle \overline{f} \rangle. \tag{2.8}$$

For example, the global-averaged streamwise velocity is $U(y) = [u]_g$.

Flow decomposition

A useful statistical tool for time-periodic flows is the three-component decomposition first introduced by Reynolds and Hussain (1972). For our spatially periodic flow, the decomposition is adapted as follows (Ricco and Hahn, 2013):

$$\mathbf{u}(x,y,z,t) = \mathbf{U}(y) + \mathbf{u_d}(x_s(x), y, z_s(z)) + \mathbf{u_t}(x,y,z,t), \tag{2.9}$$

$$\mathbf{u_d}(x_s, y, z_s) = \{u_d, v_d, w_d\} = [\overline{\mathbf{u}}]_s - \mathbf{U}(y), \tag{2.10}$$

$$\frac{\partial p}{\partial x}(x,y,z,t) = \frac{\mathrm{d}P}{\mathrm{d}x} + \frac{\partial p_d}{\partial x}(x_s(x), y, z_s(z)) + \frac{\partial p_t}{\partial x}(x,y,z,t), \tag{2.11}$$

where the mean pressure gradient $\mathrm{d}P/\mathrm{d}x$ is constant in fully-developed conditions and $\mathbf{U}(y) = \{U(y), 0, 0\}$. For clarity, we express the symmetry-average coordinates x_s, z_s as functions of the physical coordinates x, z. The flow field $\{\mathbf{u_d}, p_d\}$ is named the ring flow, while $\{\mathbf{u_t}, p_t\}$ indicates the fluctuating flow field. The governing equations for these quantities are obtained in the Appendix by applying the averaging operators to the full Navier-Stokes equations. A relation of central importance is found by substituting the decomposition (2.9) in the definition of the x-y Reynolds stresses:

$$[uv]_g = \langle u_d v_d \rangle + [u_t v_t]_g \,, \tag{2.12}$$

which appears in the mean-flow equation (A.3).

Definition of turbulent drag reduction

The separation of scales typical of wall-bounded turbulence is measured by the friction Reynolds number $Re_\tau = h^*/\delta_\nu^*$, where $\delta_\nu^* = \nu^*/u_\tau^*$ is the near-wall viscous length scale, $u_\tau^* = \sqrt{\tau_w^*/\rho^*}$ is the wall-friction velocity, $\tau_w^* = \nu^* \rho^* \mathrm{d}U^*/\mathrm{d}y^*|_{y=0}$ is the global-averaged wall-shear stress, and ρ^* is the density of the fluid. The skin-friction coefficient is $C_f =$

$2\tau_w^*/\rho^* U_b^{*2}$, where $U_b = \int_0^1 U(y)\mathrm{d}y = 2/3$ is the bulk velocity. The drag reduction $\mathcal{R}$ is defined as the percentage decrease of the skin-friction coefficient:

$$\mathcal{R}(\%) = 100(\%) \cdot \frac{C_f^0 - C_f}{C_f^0}, \tag{2.13}$$

where C_f^0 is the skin-friction coefficient of the uncontrolled flow. We also define a spatially dependent turbulent drag reduction as follows:

$$\mathcal{R}_{xz}\left(x_s, z_s\right)(\%) = 100(\%) \cdot \frac{C_f^0 - c_f\left(x_s, z_s\right)}{C_f^0}, \tag{2.14}$$

where

$$c_f\left(x_s, z_s\right) = \frac{2}{Re_p U_b^2} \left.\frac{\partial(U + u_d)}{\partial y}\right|_{y=0}. \tag{2.15}$$

It follows that $\langle \mathcal{R}_{xz} \rangle = \mathcal{R}$ because $\langle c_f \rangle = C_f$, which is a direct consequence of $\langle u_d \rangle = 0$, given by the definitions (2.10) of u_d and (2.8) of U.

Uncertainty analysis

The sampling uncertainty is estimated via normal confidence intervals, corrected for the presence of temporal correlation by fitting an auto-regressive model to the time series of the sampled variable (von Storch and Zwiers, 2001; Oliver et al., 2014). The uncertainty is first computed for the wall-shear stress τ_w^0 in the reference conditions, i.e., ϵ_0, and for the reduced wall-shear stress τ_w, i.e., ϵ. The uncertainty ϵ_R of the drag reduction $\mathcal{R}$ is then found as follows:

$$\epsilon_R = 1 - \frac{\mathcal{R}}{100} - \frac{\tau_w - \epsilon}{\tau_w^0 + \epsilon_0} \tag{2.16}$$

Table 2 presents the uncertainty values.

Table 2: Confidence intervals (95%) of the wall-shear stresses τ_w^0 and τ_w, i.e., ϵ and ϵ_0, respectively, and of the drag reduction $\mathcal{R}$, i.e., ϵ_R.

	Reference flow	**R**	**ROC**	**RHS**
$100\epsilon_0/\tau_w^0$, $100\epsilon/\tau_w$	$\pm 0.7\%$	$\pm 0.3\%$	$\pm 0.5\%$	$\pm 0.5\%$
ϵ_R	$-$	$\pm 0.9\%$	$\pm 0.9\%$	$\pm 0.9\%$

Results

Ring flow

The main features of the non-uniform ring flow $\mathbf{u_d}$ are discussed in this section. Some visualizations of $\mathbf{u_d}$ for the case without distributed control (case R) are shown in Figs.

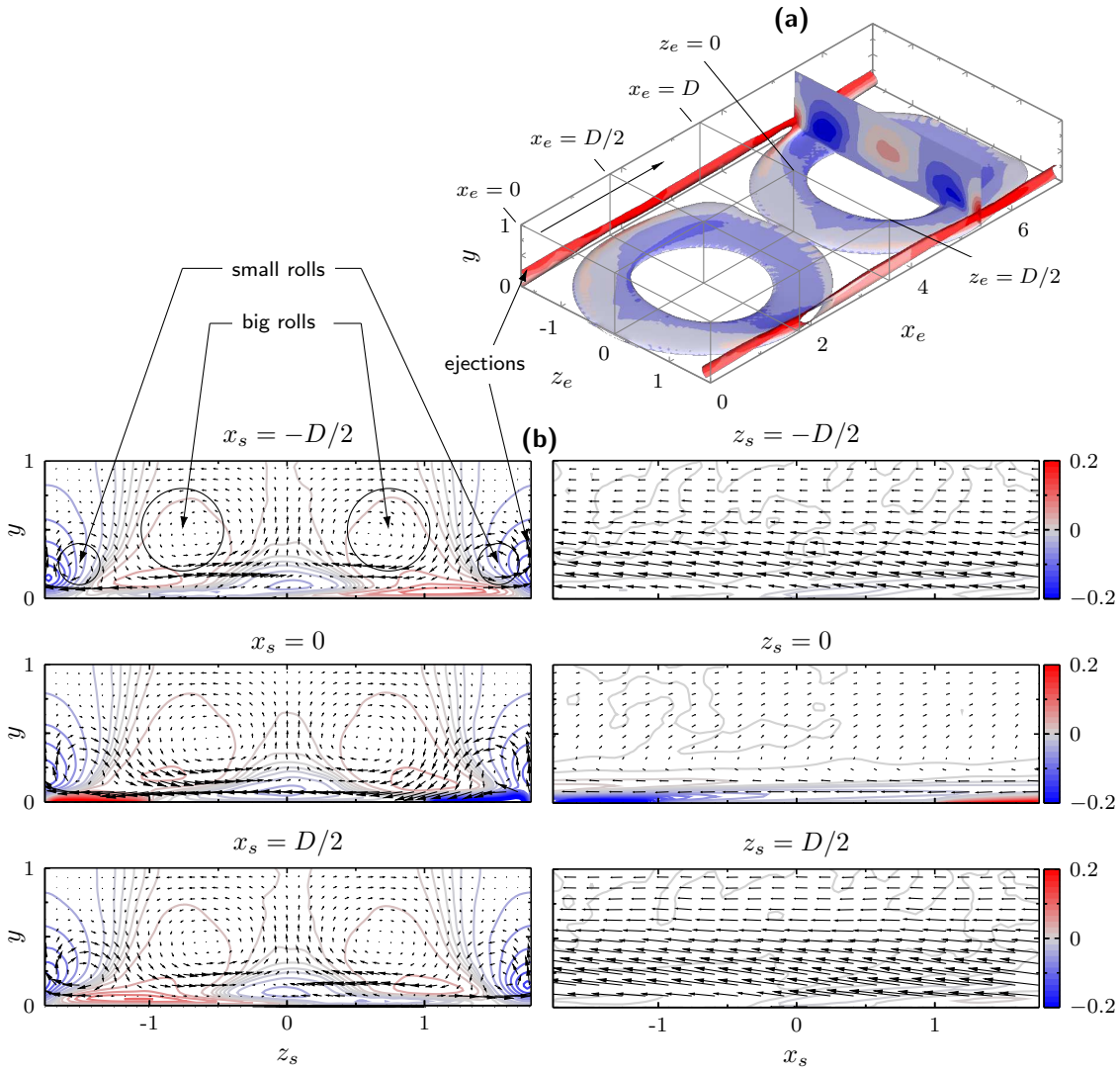

Figure 3: Rings-only flow (case R in Tab. 1). (a) The isosurface represents the magnitude $|\mathbf{u_d}| = 0.1$ and the colors show the wall-normal velocity v_d on the isosurface and on the $y - z$ plane. (b) Symmetry-averaged ring-flow $\mathbf{u_d}(\mathbf{x}_s)$ on three cross-flow planes (left graphs) and three streamwise planes (right graphs). The in-plane components are represented by the arrows and the third component is quantified by the colors of the contours. The scale of the arrows in the right column is three times smaller than in the left column. The abscissa axes span one diameter in length.

3 and 4. The three-dimensional contour plot of Fig. 3a clearly shows that the ring flow $\mathbf{u_d}$ mainly consists of the near-wall swirling motion above the rings and streamwise-elongated structures at the sides of the rings. The isosurfaces represent the magnitude of the velocity vector $|\mathbf{u_d}| = 0.1$, while the color shows v_d. The structures are mainly characterized by wall-normal and upstream ejections. Over the rotating annular actuators, the wall-normal ring-flow velocity is directed towards the wall. These features were also observed in the full-disc case (Ricco and Hahn, 2013; Wise and Ricco, 2014; Wise et al., 2014, 2018), although they have not been described exhaustively. The swirling motion on top of the rings is due to the diffusive shearing action of the rings, while the elongated structures are caused by the interaction of the radial flows of two spanwise-adjacent rings and by the radial flows encountering the stationary surface at the outer ring edge. The radial flow is produced by the wall-normal pressure gradient that draws fluid towards the wall on top of the rotating parts and then toward the outer edge of the rings. This is a consequence of the centrifugal acceleration of the fluid near the wall and it is analogous to the three-dimensional swirling laminar flow over a rotating infinite plane (von Kármán, 1921).

The streamwise component u_d exhibits a near-wall region of negative values centered at $z_s = D/2$ and confined below $y = 0.2$. Above this region, it acquires weakly positive values directly above the central region of the ring and a narrower, intensely negative region between spanwise-adjacent rings, as shown in the left graphs of Fig. 3b in cross-sectional planes perpendicular to the mean flow and in the right graphs of Fig. 3b in planes parallel to the streamwise direction. These u_d-regions balance one another because of continuity, i.e., the net flow rate of u_d across y-z planes, is null.

On x-y planes between rings (right column in Fig. 3b), the wall-normal ring-flow component v_d shows large positive values corresponding to ejections towards the channel core. These ejections persist in the streamwise direction and largely correspond to the low-speed regions of u_d, forming the streamwise-elongated structures between the rings, depicted in Fig. 3a. The product $u_d v_d$ is thus negative where these structures exist, sharing the same sign of the turbulent Reynolds stresses $\overline{u_t v_t}$. Above the spinning portion of the rings, v_d acquires negative values because it balances the intense positive ejections at the sides of the rings and the weaker positive motion toward the portion of stationary wall above the center of the rings, as shown in Fig. 3b. These positive and negative regions of v_d cancel one another out over wall-parallel planes as $\langle v_d \rangle = 0$. This alternating suction/ejection pattern induces four coherent streamwise rolls, visualized by the $v - w$ vectors of Fig. 3b (left graphs). Two of these vortices are small and intense, appearing close to the blue region of negative u_d and to the red region of positive u_d, while the other two rolls are larger and weaker, existing over the central region of the rings and located at around $y = 0.5$. These larger rolls produce the weak upward motion directly over the centerline of the ring. All four rolls are persistent in the streamwise direction as they are observed in all the cross-stream sections of Fig. 3b (left graphs).

The upstream-rotating side of the ring is responsible for the creation of intense wall-normal gradients of u_d. Fig. 4a shows that, as the upstream-moving side meets the incoming mean flow, it gives rise to a local stagnation point in the vicinity of the wall

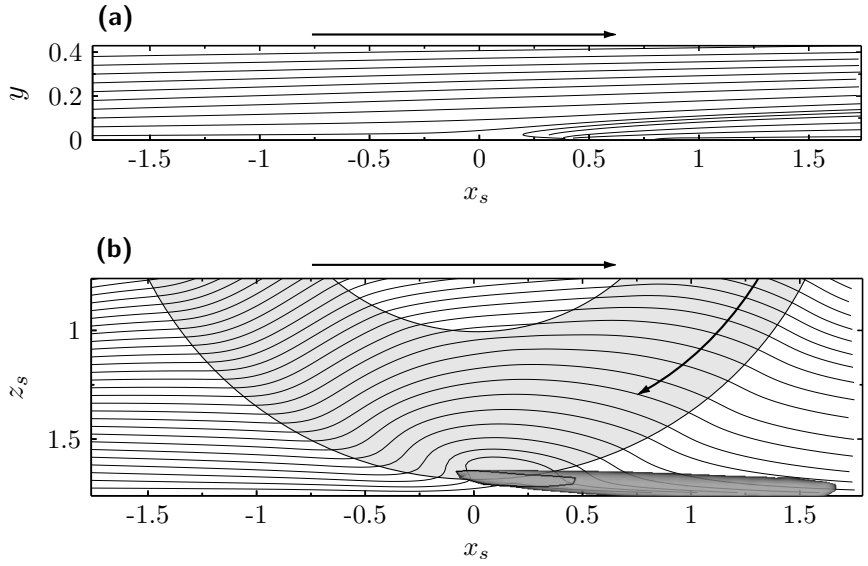

Figure 4: Rings-only flow (case R in Tab. 1). (a) Streamlines of $\mathbf{u_d}+\mathbf{U}$ in the $z_s \approx -D/2$ plane. (b) Streamlines of $\mathbf{u_d}+\mathbf{U}$ in the $y = 0.04$ plane. The dark gray three-dimensional structure is an isosurface where $|\mathbf{u_d}| = 0.14$ and $u_d < 0$.

where $U + u_d = 0$. This stagnation point moves away from the wall as the spanwise distance increases from the ring center and u_d grows from $-0.6W$ at the inner-ring edge to $-W$ at the outer-ring edge. Between these points and the wall a region of upstream motion thus occurs, while above the stagnation points the downstream flow is restored. The dark gray three-dimensional contour in Fig. 4b shows the region where u_d is most negative. This corresponds to the center of the upstream-flow region and occurs downstream of the ring.

As illustrated in Fig. 2, along the centerline of the rings the wall velocity distribution matches a triangular wave of spanwise velocity, with the exception of the stationary-wall central regions. This wave-pattern is analogous to that induced by the standing spanwise-velocity waves studied by Viotti et al. (2009) and Quadrio et al. (2009). For the rings, the equivalent wavelength is $2D^*$, which translates to about $1200\delta_\nu^*$. At comparable wavelength, Reynolds number, and forcing amplitude, the standing waves lead to their maximum drag reduction of about 45% (Viotti et al., 2009; Hurst et al., 2014). It is therefore useful to inspect the spanwise velocity profile w_d along the ring centerline at different streamwise locations. Figure 5 shows that these profiles qualitatively resemble the generalized Airy-function Stokes-layer profiles studied by Quadrio and Ricco (2011), and that, in the three control cases, they collapse on one another, irrespectively of the type of distributed forcing. This thus proves that the distributed control does not interfere with the beneficial drag-reducing action of the spinning rings because the viscous streamwise-modulated layer is unaffected when opposition control or hydrophobicity is imposed.

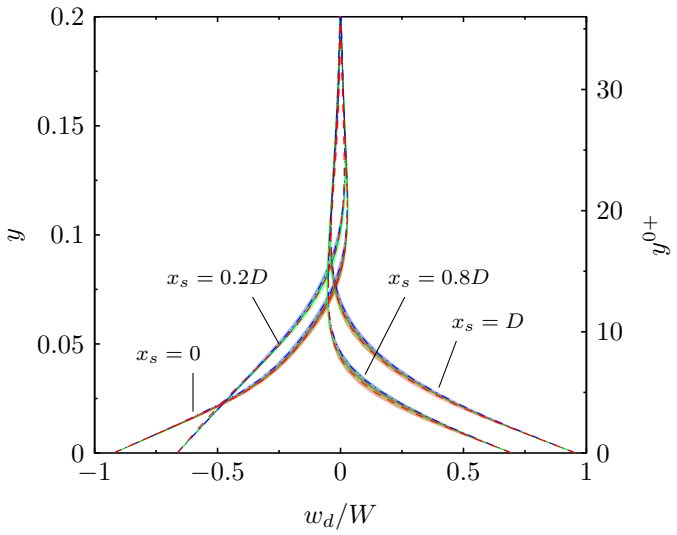

Figure 5: Profiles of the spanwise ring-flow velocity w_d at different x_s locations along the centerline of a ring. The shaded regions denote the uncertainty of the time-averaged field. Legend: —— R case; - - - ROC case; -·-·- RHS case.

It is also relevant to quantify the thickness of this viscous layer. It has been shown by Quadrio and Ricco (2011) for the standing and traveling sinusoidal waves that the drag reduction scales linearly with the wall-normal penetration length, which quantifies the thickness of the boundary layer created by wall motion. In the present case, we define this length as $\delta = -\langle w_d(y=0)/w_d'(y=0)\rangle_{x,c}$, where $\langle\cdot\rangle_{x,c}$ denotes the spatial average along the centerline of the ring where $w_d(y=0) \neq 0$ and the prime symbolizes differentiation with respect to the wall-normal direction. We find that the penetration depth is $\delta^+ = 6.5$ in all the cases, which matches to the optimal value found by Quadrio and Ricco (2011) for the sinusoidal-wave forcing.

Turbulence statistics

Figures 6 and 7 present the wall-normal statistical profiles scaled in the reference wall units, i.e., by u_τ^* and δ_ν^* (superscript 0+), and scaled in native wall units, i.e., by u_τ^* and δ_ν^* of each drag-reduced flow (superscript +), respectively. Drag reduction is shown in Fig. 6a for the R and ROC cases ($\mathcal{R} = 20\%$ and $\mathcal{R} = 27.4\%$) as a lower streamwise velocity is computed in the viscous sublayer. The skin-friction coefficient also drops in the RHS case ($\mathcal{R} = 26.5\%$), but this is not immediately evident due to the wall-slip velocity. As the flow rate is constant, the R and ROC profiles display slightly larger velocity in the outer layer due to the near-wall reduced flow rate. The RHS profile shows lower velocities near the centerline, balancing the increased near-wall velocity due to the hydrophobic slip. The inception of the logarithmic layer shifts upwards, denoting a thicker viscous sublayer. The mean profiles shift upward above the viscous sublayer

when scaled with their native wall-friction velocities, as shown in Fig. 7.

The turbulent fluctuations are significantly attenuated. Both the $[u_t u_t]_g^{0+}$ profiles in Fig 6b and the $[uv]_g^{0+}$ profiles in Fig. 6c are reduced mostly up to $y^{0+} = 100$. ROC is the most effective in decreasing $[uu]_g^{0+}$ and $[uv]_g^{0+}$, although the latter increases in the viscous sublayer because of the enhanced wall-normal velocity fluctuations. The wall-normal peaks of $[u_t u_t]_g^{0+}$ are shifted away from the wall by about $10\delta_\nu^*$ with respect to the reference case. The components of $[uv]_g^{0+}$, defined in (2.12), are shown in Fig. 6d. Since $[u_d v_d]_g^{0+}$ is negative over most of the channel height, the coherent streamwise and wall-normal ejections between spanwise-adjacent rings increase the drag. The turbulent Reynolds stresses $[u_t v_t]_g^{0+}$ are instead strongly suppressed, showing the beneficial drag-reducing influence of the rings. The cases with distributed forcing are observed to further weaken the total Reynolds stresses with respect to the rings-only case. The ROC $[u_d v_d]_g^{0+}$ profiles are weaker than in the rings-only case, whereas in the RHS case they are more intense than in the rings-only case outside the near-wall region. All the native-scaled profiles are lower than in the fixed-wall condition. This is due to the lower native Re_τ caused by drag reduction and to the wall-bounded flow being altered with respect to the reference flow.

The wall-normal turbulent $[\overline{u_t v_t}]_s^{0+}$ profiles, shown in Fig. 8 at fixed x_s, z_s locations, are significantly non-uniform along z_s. The Reynolds stresses along the ring centerline are significantly diminished by the spanwise wave-like motion caused by the rings. The opposite behaviour characterizes the ring sides, where the strengthened Reynolds stresses reach peaks up to 150% of the reference case. These regions are narrower than those where the stresses are weakened, so the global effect is a reduction. The profiles (b) and (d) of Fig. 8 are representative of the central middle 60% of a ring. The two types of distributed control act differently and not uniformly, especially at location (a), i.e., over the stationary wall surface confined between four adjacent rings. Here ROC yields lower $[\overline{u_t v_t}]_s^{0+}$ peaks, while RHS is not very effective in reducing the fluctuations. In the region confined within the rings, the distributed controls offer little additional damping of the turbulent fluctuations compared to the R case as the turbulence intensity is already low.

Fig. 9 illustrates, via the λ_2 invariant (Jeong and Hussain, 1995), the fine-scale turbulent structures in the reference case and in the drag-reduced cases. The vortices are almost absent in the central region over the rings, in stark contrast with the more intense vortices on the streamwise-elongated structures between rings. These visualizations are consistent with the profiles of Fig. 8, which show the intense non-uniformity of the Reynolds stresses along the spanwise direction.

Turbulent drag reduction

In this section, the turbulent drag reduction generated by the spinning motion of the rings combined with the effects of the opposition control and the hydrophobic surfaces is examined, both globally and locally in space. The contribution of the different terms of the Navier-Stokes equations to the drag reduction is studied through an extended form of the Fukagata-Iwamoto-Kasagi identity (Fukagata et al., 2002).

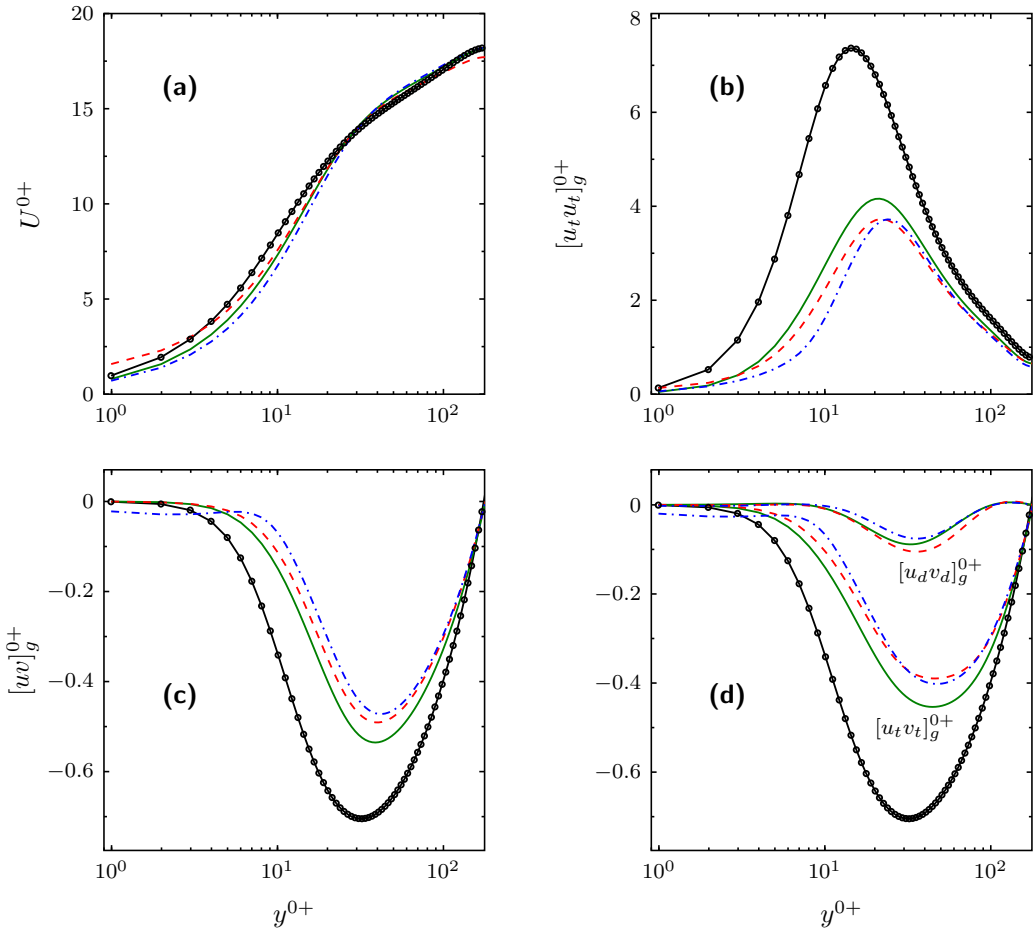

Figure 6: Wall-normal profiles of the turbulent statistics, scaled in wall units of the reference channel flow. (a) Mean velocity. (b) Streamwise turbulent intensity. (c) Total Reynolds shear stress. (d) Reynolds stress decomposition according to (2.12). Color key: reference channel flow; R case; ROC case; RHS case.

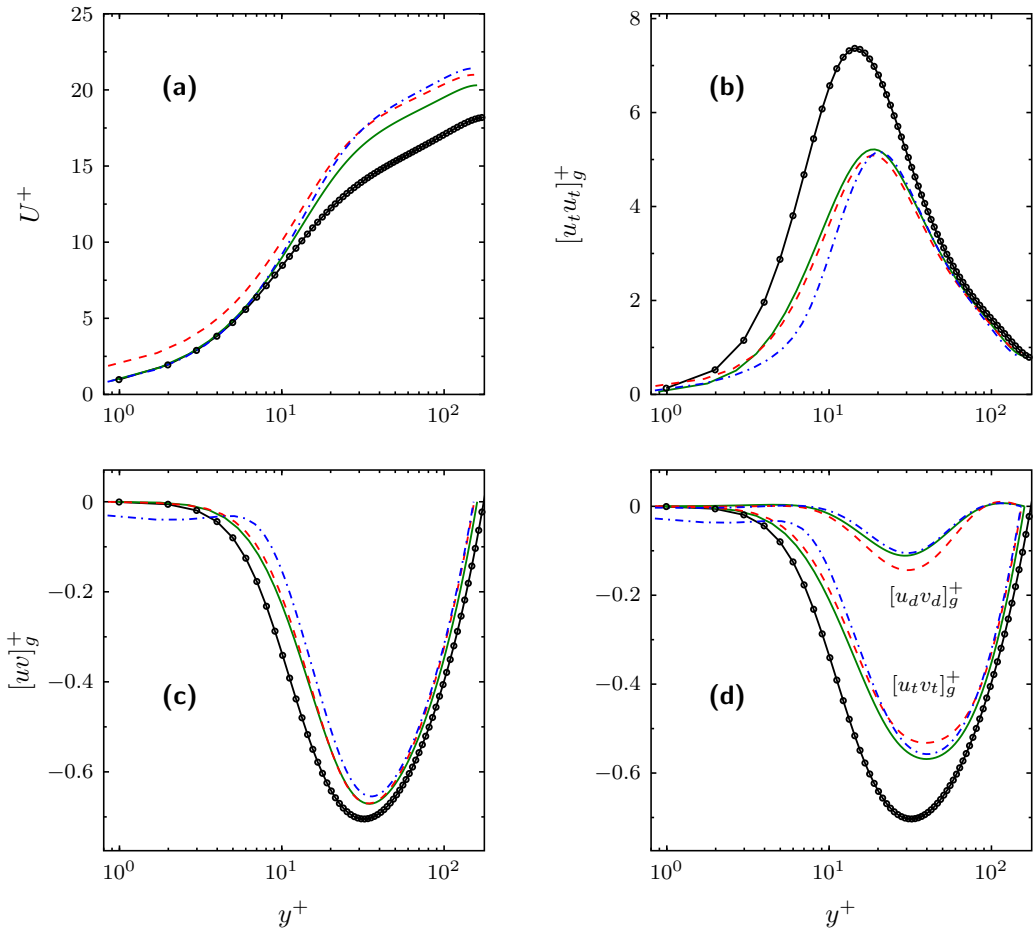

Figure 7: Wall-normal profiles of the turbulent statistics, scaled in native wall units. (a) Mean velocity. (b) Streamwise turbulent intensity. (c) Total Reynolds shear stress. (d) Reynolds stress decomposition according to (2.12). Color key: —o— reference channel flow; —— R case; - - - ROC case; -·-·- RHS case.

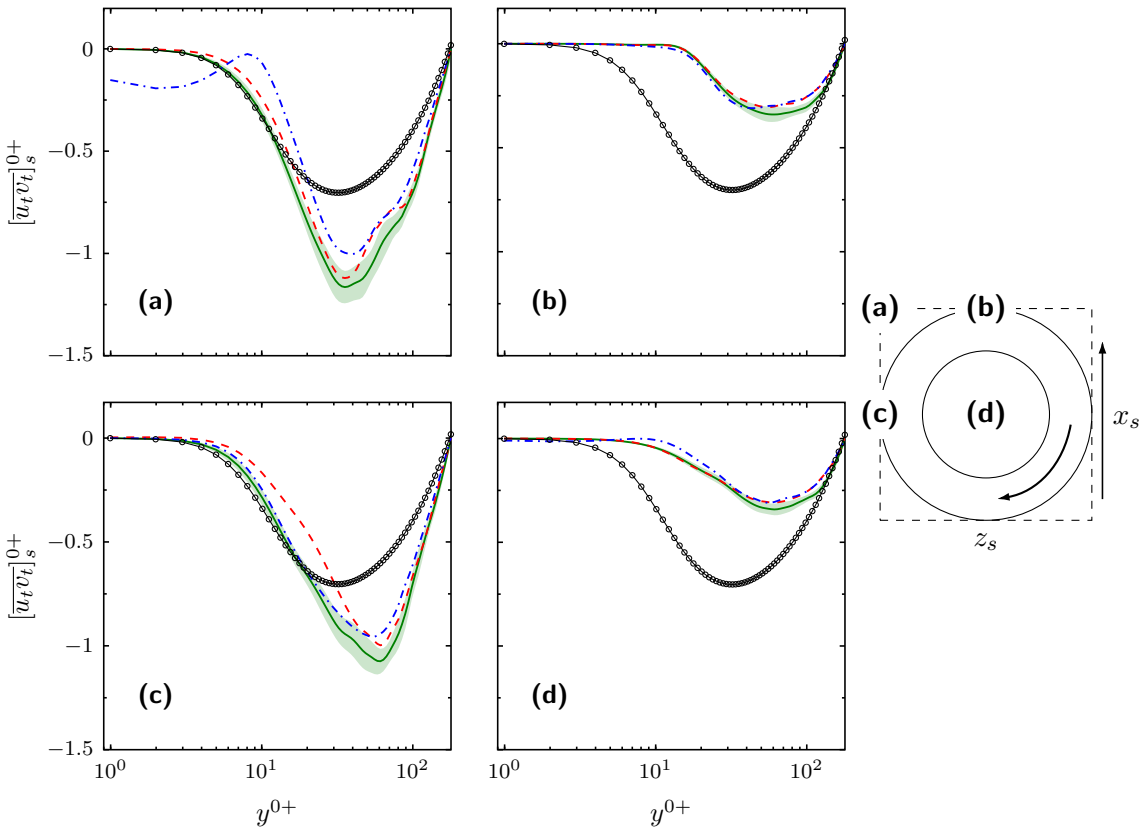

Figure 8: Turbulent Reynolds stress profiles at different positions in the symmetry-averaged frame. The variables are scaled with the wall units of the reference channel. The locations are letter-coded as in the sketch on the right. Color key: —o— reference channel flow; —— R case; - - - ROC case; -·-· RHS case. The shaded green regions denote the uncertainty of the time-averaged field.

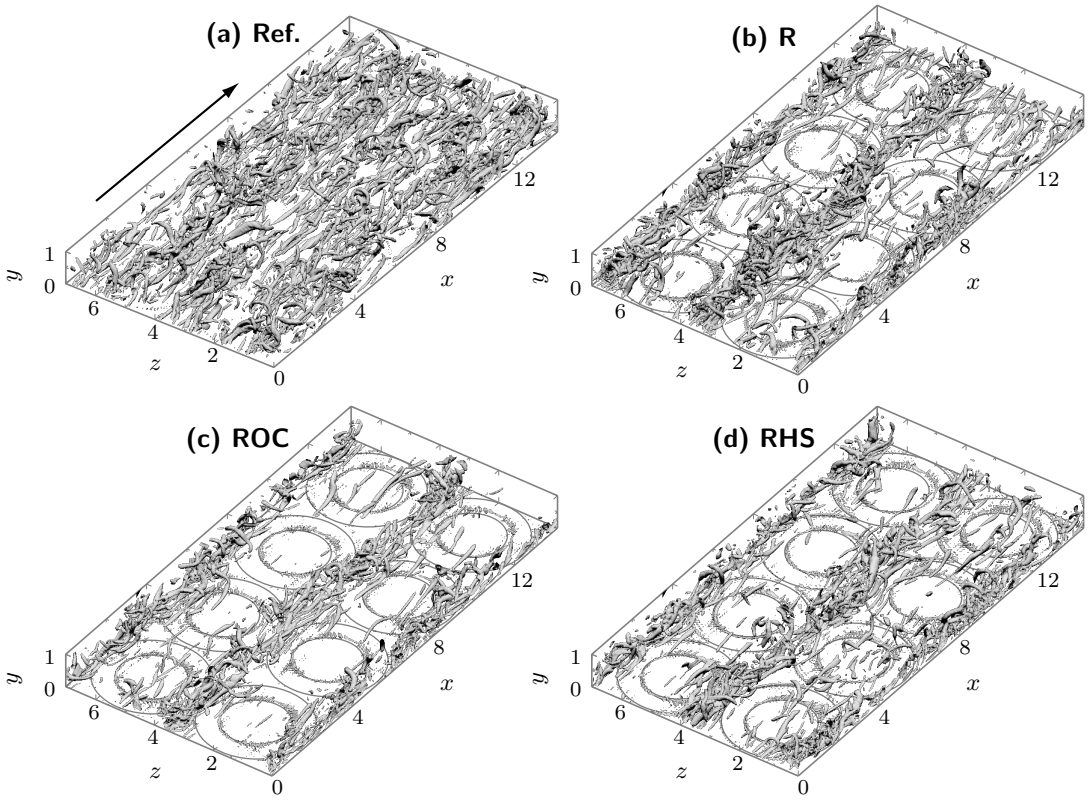

Figure 9: Instantaneous λ_2^+-isocontours at $\lambda_2^{0+} = -0.007$. (a) reference flow, (b) rotating rings, (c) rotating rings and opposition control, (d) rotating rings and hydrophobic surface.

Ideal prediction of combined-forcing drag reduction

We first predict the turbulent drag reductions $\mathcal{R}_{id}$ generated by the combination of the rings and the distributed controls and compare these ideal predictions with the values computed via the direct numerical simulations. We use two assumptions:

1. For the first assumption, we consider the drag reduction generated by the distributed controls without the spinning rings. We assume that the reduction of the total drag is obtained by multiplying the fraction of actuated area by the drag reduction obtained if the whole surface area were altered by the distributed control, irrespectively of the geometrical arrangement of the controlled area.

2. For the second assumption, we first consider the wall-turbulent flow altered by the distributed actuation imposed over the area not occupied by the stationary rings. We assume that the action of the rings on this drag-reduced flow leads to the same amount of drag reduction $\mathcal{R}_R$ as if the rings operated on the reference turbulent

channel flow without control. This assumption is directly related to the spanwise ring-flow not being influenced by the distributed actuation, as demonstrated in Fig. 5.

It is useful to introduce the following definitions. We define $\mathcal{R}_{\text{dis-tot}}$ as the drag reduction via distributed control when the whole wall is actuated, $C_{f,1}$ as the skin-friction coefficient obtained via the distributed control activated over the area not occupied by the rings when the rings are not in motion, and $C_{f,2}$ as the skin-friction coefficient produced by the combination of the rings and the distributed control. The ratio between the combined skin-friction coefficient $C_{f,2}$ and the uncontrolled value C_f^0 is written as:

$$\frac{C_{f,2}}{C_f^0} = \frac{C_{f,2}}{C_{f,1}} \cdot \frac{C_{f,1}}{C_f^0}. \tag{3.1}$$

According to the first assumption:

$$\frac{C_{f,1}}{C_f^0} = 1 - \frac{\mathcal{R}_{\text{dis-tot}} S_{\text{dis}}}{S_{\text{tot}}}, \tag{3.2}$$

where S_{dis} is the area not occupied by the rings and $S_{\text{tot}} = L_x L_z$ is the total surface area. According to the second assumption:

$$\frac{C_{f,2}}{C_{f,1}} = 1 - \mathcal{R}_R. \tag{3.3}$$

Substitution of (3.2) and (3.3) into (3.1) leads to:

$$\mathcal{R}_{id} = \mathcal{R}_R + \frac{\mathcal{R}_{\text{dis-tot}} S_{\text{dis}}}{S_{\text{tot}}} - \mathcal{R}_R \frac{\mathcal{R}_{\text{dis-tot}} S_{\text{dis}}}{S_{\text{tot}}}. \tag{3.4}$$

The equation (3.4) shows that the predicted drag reduction is equal to the sum of the drag reductions produced by the two methods as if they operated separately minus the last term on the right representing the ideal loss. In our idealized model, this loss accounts for the drag reduction effect caused by the rings operating on a wall-bounded flow with a skin-friction coefficient that is lower than the reference one. We quantify the non-ideal interaction between the rings and the distributed control by defining the difference between the drag reduction computed via the direct numerical simulations and the ideal prediction given by (3.4):

$$\Delta\mathcal{R} = \mathcal{R} - \mathcal{R}_{id}. \tag{3.5}$$

The difference $\Delta\mathcal{R}$ arises mainly because the second assumption is not fully applicable, i.e., the effects of non-uniformity of the drag-reduced flow caused by the distributed forcing alone and by the ring-flow being altered by the distributed control between spanwise-adjacent rings.

Table 3: Drag reduction values obtained by the combination of the rings and the distributed controls.

	Rings	**OC**	**HS**	**ROC**	**RHS**	**OCR0**	**HSR0**
$\mathcal{R}(\%)$	20.0	23.3	27.7	27.4	26.5	11.5	13.2
$\mathcal{R}_{id}(\%)$	-	-	-	29.3	31.1	11.7	13.8
$\Delta\mathcal{R}(\%)$	-	-	-	-1.9	-4.6	-0.2	-0.6

Table 3 reports the values of the numerically-computed $\mathcal{R}$, the predicted $\mathcal{R}_{id}$, and their difference $\Delta\mathcal{R}$. For the distributed control cases with stationary rings, OCR0 and HSR0, $\mathcal{R}_{id}$ is calculated by adopting the first assumption, i.e., by multiplying the $\mathcal{R}$ values given by the full-wall OC and HS controls by the fraction of actuated area $S_{\rm dis}/S_{\rm tot}$. These ideal values agree well with the numerically computed ones, i.e., within 95% confidence intervals, especially the opposition-control values. These agreements support the first assumption. In the combined cases, the drag reduction $\mathcal{R}$ increases by a similar amount with respect to the rings-only case, i.e. 7.4% in the ROC case and 6.5% in the RHS case. However, neither fulfils the ideal expectation as $\Delta\mathcal{R} < 0$ in both cases. As these values are negative, the ideal estimate (3.4) represents an upper bound for the combined-forcing drag reduction. The $\Delta\mathcal{R}$ values in the ROC and RHS cases are comparable in magnitude and larger than the estimated uncertainties (refer to Table 2), but the agreement between the predicted and the numerical values is satisfactory. The discrepancy is larger in the hydrophobic-wall case than in the opposition-control case: the predicted drag reduction value is about 17% larger than the numerical value, whereas in the ROC case the prediction is about 6.5% higher than the computed value.

Spatial distribution of drag reduction

The contour maps of Fig. 10 show $\mathcal{R}_{xz}$, defined in (2.14), for the rings-only case (Fig. 10a), the differences between $\mathcal{R}_{xz}$ in the rings-only case and in the two combined-forcing cases (Fig. 10b,c), and the differences between the numerical $\mathcal{R}_{xz}$ values in the combined-forcing cases and the predicted $\mathcal{R}_{xz,id}$, defined as

$$\mathcal{R}_{xz,id} = \mathcal{R}_{xz,R} + \mathcal{R}_{xz,OC/HS} - \mathcal{R}_{xz,R}\mathcal{R}_{xz,OC/HS}, \tag{3.6}$$

where $\mathcal{R}_{xz,OC/HS}$ is $\mathcal{R}_{xz}$ generated by the opposition control or the hydrophobic control applied over the area not covered by the rings. These differences highlight the regions where the drag reduction is markedly altered with respect to the rings-only case. The spatial distribution of the time- and ensemble-averaged wall-shear stress reduction is strongly non-uniform and depends on the type of distributed forcing.

Fig. 10a shows that $\mathcal{R}_{xz,R}$ is determined by the rotation on the ring surface, thus negative on the upstream-rotating half (drag increase, blue color) and positive on the downstream-rotating half (drag reduction, red color). The red positive-$\mathcal{R}_{xz}$ region on the rotating ring surface is larger than the blue negative-$\mathcal{R}_{xz}$ region. The stationary

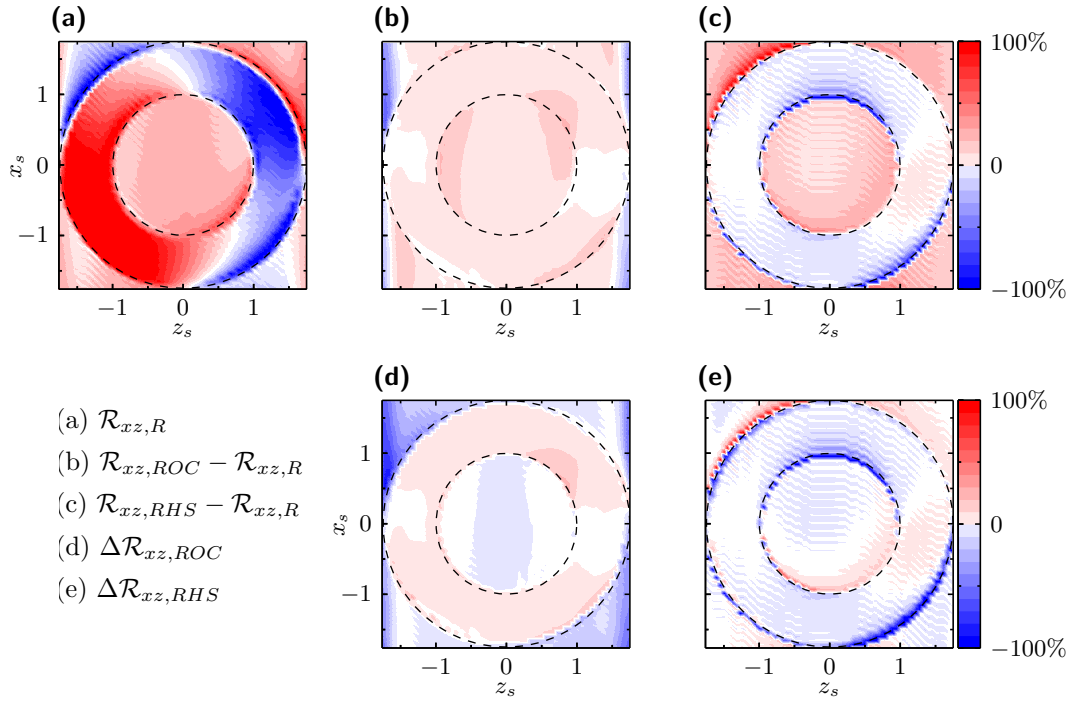

Figure 10: Spatial distribution of (a) the drag reduction $\mathcal{R}_{xz}$ for the rings-only case, the difference between $\mathcal{R}_{xz}$ in the rings-only case and the ROC and the RHS cases, (b) and (c) respectively, and the differences between $\mathcal{R}_{xz}$ for the ROC and the RHS cases and the predicted $\mathcal{R}_{xz,id}$, (d) and (e) respectively.

inner-ring region benefits from levels of drag reduction as high as 40% and the wall-shear stress distribution is quite uniform. It is therefore not directly influenced by the ring sides spinning in opposite directions. The region outside of the ring is largely dominated by the combined effects of the radial swirling flow, the interaction between adjacent rings, and the adjustment of the flow from the rotating portion of the wall and the stationary surface. Drag reduction is observed downstream of the upstream-rotating part of the ring, whereas drag increase occurs downstream of the downstream-rotating part of the ring. The drag is reduced upstream of the downstream-rotating side of the ring and increases upstream of the upstream-rotating side. On the lateral strips located directly underneath the ejections/low-speed regions, $\mathcal{R}_{xz,R}$ takes highly positive values. This proves that the streamwise-elongated structures have a direct but spatially limited beneficial effect on the wall-shear stress reduction, although their associated ring-flow Reynolds stresses are negative, as shown in Fig. 6d.

Fig. 10b shows that the combined forcing ROC yields about 10% more drag reduction in the inner-ring region than the rings-only case and has a similar beneficial effect on the large portions of the rotating rings, although it is not applied there. The bands between spanwise-adjacent rings experience a drag increase of up to 27% with respect to $\mathcal{R}_{xz,R}$, consistently with the weaker ring-flow structures in the ROC case, as displayed in Fig. 6d. Fig. 10c shows that the drag reduction $\mathcal{R}_{xz}$ of the RHS case is less uniform than the ROC case. Therefore, their similar $\mathcal{R}$ values, reported in table 3, do not reveal the markedly different physics. In the inner region, the RHS case delivers an improvement of about 15% drag reduction with respect to the rings-only case, which is much larger than in the ROC case. Outside of the ring, RHS has a uniform beneficial effect on the drag reduction. On the rotating region instead the average drag increases.

Several studies (e.g. Min and Kim (2004)) have established that in the reference channel flow the level of drag reduction depends on U_s^+, the mean slip velocity scaled in native wall units. In the full-wall hydrophobic case, $U_s^+ = 3$. The global drag reduction achieved by the HSR0 case is very close to its $\mathcal{R}_{id}$, as shown in Table 4, and the mean slip velocity is very close to $U_s^+ = 3$ when scaled with the viscous length obtained from the averaged wall-shear stress over the hydrophobic surface. This supports the hypothesis that when the rings are not rotating, the ideal prediction is accurate. In the combined RHS case the slip velocity is smaller, i.e., $U_s^+ = 2.65$ in the central region, which is consistent with the intense reduction of wall-shear stress induced by the ring rotation.

The contours 10d and 10e depict the difference between the numerical $\mathcal{R}_{xz}$ and the ideal $\mathcal{R}_{xz,id}$, defined in (3.6). In the ROC case, the $\mathcal{R}_{id}$ overpredicts the numerical value over the regions not occupied by the rings, whereas the opposite occurs on the ring surface. In the RHS case, the difference is more non-uniform than the ROC case and the streamwise increase/reduction pattern along the streamwise direction is due to the local adjustment of the flow from the finite-slip over the hydrophobic surface to the no-slip condition on the ring surface and vice-versa.

Decomposition through the Fukagata-Iwamoto-Kasagi identity

In this section we examine the relation between the spatially-dependent skin-friction coefficient c_f defined in (2.15) and the terms of the Navier-Stokes equations to understand the origin of drag reduction and its spatial distribution. To this purpose, we apply the Fukagata-Iwamoto-Kasagi (FIK) theory (Fukagata et al., 2002) to our time- and ensemble-averaged streamwise momentum equation (A.2) for $\mathbf{U}+\mathbf{u_d}$. This leads to the following integral identity for the spatially-dependent skin-friction budget:

$$\begin{aligned} c_f(x_s,z_s) = &\underbrace{\frac{6}{Re_p U_b}}_{C_f^{\mathrm{lam}}} \underbrace{-\frac{6U(0)}{Re_p U_b^2}}_{C_f^s} \underbrace{-\frac{6}{U_b^2}\int_0^1 (1-y)u_d v_d \mathrm{d}y}_{c_f^d} \underbrace{-\frac{6}{U_b^2}\int_0^1 (1-y)\left[\overline{u_t v_t}\right]_s \mathrm{d}y}_{c_f^t} \\ &\underbrace{+\frac{6}{Re_p U_b^2}\int_0^1 (u_d - u_{d,0})\,\mathrm{d}y}_{c_f^{ud}} \underbrace{-\frac{3}{U_b^2}\int_0^1 (1-y)^2 I_x''\mathrm{d}y}_{c_f^x} \underbrace{-\frac{3}{U_b^2}\int_0^1 (1-y)^2 I_z''\mathrm{d}y}_{c_f^z} \\ &\underbrace{-\frac{3}{U_b^2}\int_0^1 (1-y)^2 \mathcal{C}''\mathrm{d}y}_{c_f^{\mathcal{C}}} \underbrace{-\frac{3}{U_b^2}\int_0^1 (1-y)^2 \Pi_x''\mathrm{d}y}_{c_f^{\Pi}}, \end{aligned} \tag{3.7}$$

where c_f is defined in (2.15) and $u_{d,0} = u_d(x_s, 0, z_s)$. Following the notation adopted by Fukagata et al. (2002), the superscript $''$ indicates the difference between a quantity q and its bulk integral, as follows

$$q'' = q - \int_0^1 q \ \mathrm{d}y. \tag{3.8}$$

The last four integrals in (3.7) are defined by grouping the terms in the streamwise momentum equation (A.2) that are null when averaged over x_s and z_s, as follows:

$$I_x = \frac{\partial}{\partial x_s}\left(u_d^2 + \left[\overline{u_t^2}\right]_s - \frac{\partial u_d}{\partial x_s}\right), \tag{3.9}$$

$$I_z = \frac{\partial}{\partial z_s}\left(u_d w_d + \left[\overline{u_t w_t}\right]_s - \frac{\partial u_d}{\partial z_s}\right), \tag{3.10}$$

$$\mathcal{C} = U\frac{\partial u_d}{\partial x_s} + v_d\frac{\partial U}{\partial y}, \tag{3.11}$$

$$\Pi_x = \frac{\partial p_d}{\partial x_s}. \tag{3.12}$$

The term C_f^{lam} represents the laminar part of the skin-friction coefficient. The term C_f^s in (3.7) is non-zero only in the RHS case: it is due to the finite average wall-slip velocity caused by the hydrophobicity of the surface (Aghdam and Ricco, 2016). Its magnitude is about 2% of C_f.

Table 4: Contributions of the Reynolds-stress components to the global skin-friction budget. The values of the partial skin-friction coefficients are multiplied by 10^3 and the values of the partial drag reduction values are percentage.

	C_f	C_f^{lam}	C_f^d	C_f^t	C_f^s	$\mathcal{R}$	$\mathcal{R}_d$	$\mathcal{R}_t$	$\mathcal{R}_s$
Reference flow	8.12	2.14	-	5.97	-	-	-	-	-
Rings	6.48	2.14	0.42	3.92	-	20.0	−5.2	25.2	-
ROC	5.88	2.14	0.36	3.38	-	27.4	−4.4	31.9	-
RHS	5.96	2.14	0.53	3.41	−0.12	26.5	−6.6	31.6	1.5

The terms $c_f^d(x_s, z_s)$ and $c_f^t(x_s, z_s)$ are the contributions of the two Reynolds-stress components $u_d v_d$ and $[\overline{u_t v_t}]_s$ to the skin-friction coefficient. The terms in the second and third lines of (3.7) are zero when (3.7) is averaged along x_s and z_s. The term c_f^{ud} originates from the spatial distribution of the ring-flow streamwise component u_d. The terms c_f^x and c_f^z are related to I_x in (3.9) and I_z in (3.10), respectively, and therefore to the x-x and x-z Reynolds and viscous stresses. The term $c_f^{\mathcal{C}}$ involves $\mathcal{C}$, defined in (3.11), and thus expresses the influence of the convective transport due to the interaction between the mean flow and the ejections at the sides of the rings. The term Π_x accounts for the non-uniform part of the pressure gradient.

By averaging (3.7) along x_s and z_s, the following expression for the skin-friction coefficient is found (Ricco and Hahn, 2013):

$$C_f = C_f^{\mathrm{lam}} + C_f^d + C_f^t + C_f^s, \tag{3.13}$$

where $C_f^d = \langle c_f^d \rangle$ and $C_f^t = \langle c_f^t \rangle$. Table 4 reports the values of the terms in (3.13) for the drag-reduction cases, revealing that C_f^t exceeds C_f^d by one order of magnitude in all the cases. Table 4 also shows the partial drag reductions that add up to the total drag reduction, i.e., $\mathcal{R}_d + \mathcal{R}_t + \mathcal{R}_s = \mathcal{R}$, where $\mathcal{R}_d(\%) = -100 \cdot C_f^d / C_f^0$, $\mathcal{R}_t(\%) = 100 \cdot (C_f^0 - C_f^t)/C_f^0$, $\mathcal{R}_s(\%) = -100 \cdot C_f^s / C_f^0$, and $C_f^{t,0} = C_f^0 - C_f^{\mathrm{lam}}$. The values of $\mathcal{R}_d$ show the detrimental role of $\mathbf{u_d}$, which always increases the global drag. The analysis of the partial drag reduction budget also uncovers fundamental differences between the two combined control schemes. While both ROC and RHS can substantially reduce C_f^t to a very similar level, in the ROC case $\mathcal{R}_d$ is more than 2% smaller than in the RHS case, while in the latter case C_f^d is larger than the rings-only case.

To improve the understanding of the flow, we average the terms in (3.7) along x_s, obtaining z_s-dependent quantities. This procedure leads to a limited loss of spatial information since the turbulence statistics are approximately uniform along the streamwise direction, as evident from Fig. 8. The budget of the skin-friction coefficient becomes

$$\langle c_f \rangle_x(z_s) = C_f^{\mathrm{lam}} + C_f^s + \langle c_f^d \rangle_x + \langle c_f^t \rangle_x + \langle c_f^{ud} \rangle_x + \langle c_f^x \rangle_x + \langle c_f^z \rangle_x + \langle c_f^{\mathcal{C}} \rangle_x + \langle c_f^{\Pi} \rangle_x \tag{3.14}$$

The graphs in the first row of Fig. 11 show $\langle c_f^d \rangle_x(z_s)$ and $\langle c_f^t \rangle_x(z_s)$, thereby providing more insight into the values of Table 4.

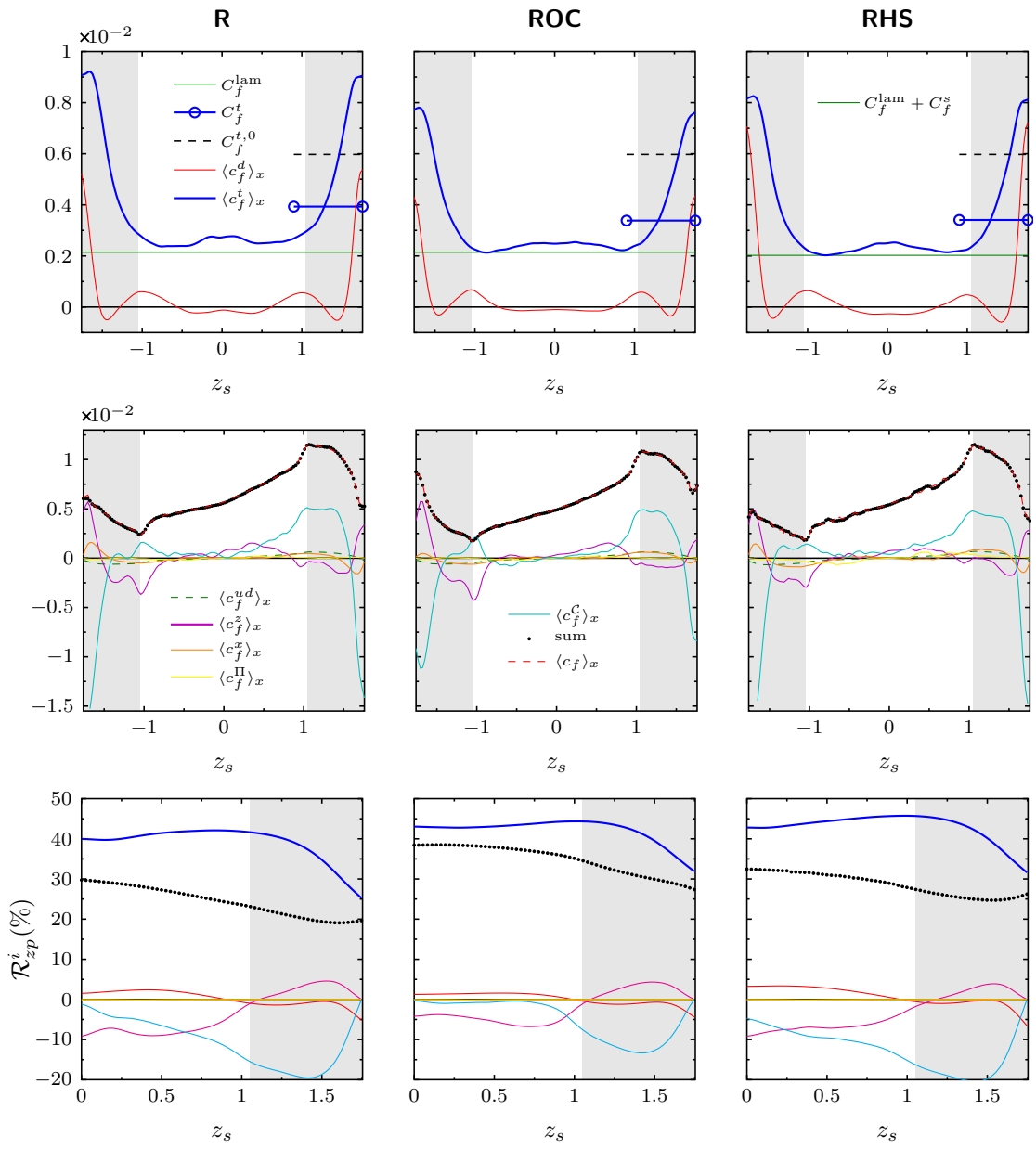

Figure 11: Spatially-dependent skin-friction budget defined in (3.14). The leftmost column is relative to rings-only control, the central column to ROC, and the rightmost column to RHS. The first row displays the first four terms of (3.14). The horizontal blue segments represent the global mean value C_f^t and the black dashed line denotes $C_f^{t,0}$. The second row displays the last three terms and the sum of all the terms of (3.14). The third row shows the progressively-averaged drag reduction, according to (3.15).

The rings-only case is first examined (left column in Fig. 11). In the central region, the viscous boundary layer induced by the ring motion, shown in Fig. 5, reduces $\langle c_f^t \rangle_x$ (blue line) by 40%, i.e., at a level similar to that given by a sinusoidal wave at the same amplitude and wavelength, whereas at the ring sides, $\langle c_f^t \rangle_x$ has peaks at the ring sides exceeding the reference channel value $C_f^{t,0}$ (black dashed line) by 150%. This detrimental effect adds up to that of $\langle c_f^d \rangle_x$ (red line) that also peaks at the same locations. In all the configurations, the peak contributions to the global C_f originate from the sides of the rings where both $\langle c_f^d \rangle_x$ and $\langle c_f^t \rangle_x$ have a maximum. Since in the central region u_d is almost uniformly positive, the sign of $u_d v_d$ is dictated by the positive wall-normal component v_d, shown in the y-z plane of Fig. 3a. In the central region, the term $\langle c_f^d \rangle_x$ thus has a mild drag-reducing influence where ejections occur and a slightly more significant drag-increasing effect beneath the sides of the central rolls.

Although most of the globally drag-increasing contributions (i.e., peaks of $\langle c_f^t \rangle_x$ and $\langle c_f^d \rangle_x$) originate from the side regions, in Fig. 10a the above-average values of $\mathcal{R}_{xz,R}$ occur between rings because the structures locally decrease the drag as u_d is negative between spanwise adjacent rings. The sum of all the terms of (3.14) (black circles in Fig. 11, second row) shows that the total $\langle c_f \rangle_x$ has a minimum on the right upstream-rotating side of the ring. This minimum is due to $\langle c_f^{\mathcal{C}} \rangle_x$ (light blue line), which has drag-reduced negative peaks that are much more intense in absolute value than the local peaks of the drag-increasing $\langle c_f^t \rangle_x$ and $\langle c_f^d \rangle_x$ in the ring-side region. This explains the narrow region of large positive $\mathcal{R}_{xz}$ at the right ring side. Once averaged along x_s, $\langle c_f^{\mathcal{C}} \rangle_x$ consists only of the term $v_d \partial U / \partial y$, i.e., the wall-normal advection of U along v_d. Therefore $\langle c_f^{\mathcal{C}} \rangle_x$ is maximum at the sides of the ring because of the lateral ejections identified in §3.1. The term $\langle c_f^z \rangle_x$ (purple line) instead contributes detrimentally to the local skin friction by the intense peak at the sides. Most of the contribution to $\langle c_f^z \rangle_x$ is due to the Reynolds stresses $[\overline{u_t w_t}]_s$. The sum of the terms (black circles) coincides with $\langle c_f \rangle_x$ calculated from the wall-normal velocity gradient at the wall (dashed red line).

Further insight is gained by the bottom graphs of Fig. 11, which show

$$\mathcal{R}_{zp}(z_s) = \frac{100(\%)}{2z_s} \int_{-z_s}^{z_s} \frac{C_f^0 - \langle c_f \rangle_x(\widehat{z}_s)}{C_f^0} \, \mathrm{d}\widehat{z}_s, \tag{3.15}$$

i.e., the progressive spanwise average of the local drag reduction from the ring centerline at $z_s = 0$ towards the edges. At $z_s = D/2$, the global drag reduction $\mathcal{R}$ is retrieved by the integral (3.15). The partial spanwise-averaged drag reduction corresponding to the terms of equation (3.14), named $\mathcal{R}_{zp}^i(z_s)$ (where i denotes the corresponding superscripts of the terms), are found by substituting these terms into (3.15). The curves of $\mathcal{R}_{zp}^t(z_s)$ demonstrate that more than 20% of the global $\mathcal{R}_R$ is lost in the side regions, while it remains essentially constant over the central region and of similar magnitude to the drag reduction produced by the standing waves (Viotti et al., 2009).

We now discuss how the wall-shear stress is modified in the ROC case by inspecting the graphs in the central column of Fig. 11. The action of OC results in a pronounced weakening of both the lateral peaks of $\langle c_f^d \rangle_x$ and $\langle c_f^t \rangle_x$, explaining the partial drag

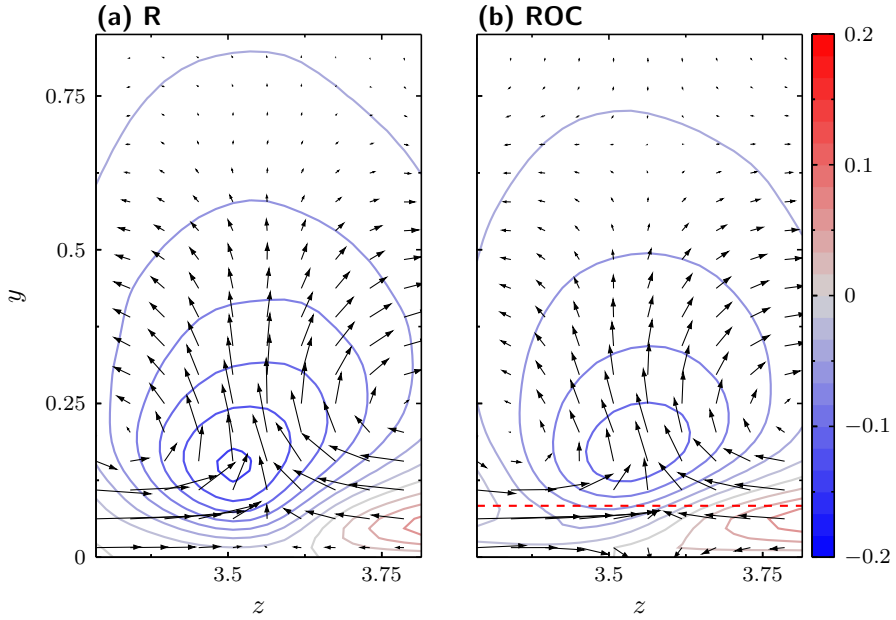

Figure 12: Action of the opposition control on $\mathbf{u}_d$, visualized on cross-stream sections at $x_s = D/2$. The contours depict the streamwise component u_d. (a) Rings-only forcing. (b) case ROC. The dashed red line marks the detection height $y_d^{0+} = 14.5$.

reductions $\mathcal{R}_t$ and $\mathcal{R}_d$ in Table 4. In the central region, $\langle c_f^t \rangle_x$ is slightly reduced with respect to the rings-only case. The progressively-averaged $\mathcal{R}_{zp}^t$ curve of Fig. 11 (bottom central graph) confirms the additional 5% reduction of $\langle c_f^t \rangle_x$ with respect to the rings-only case in the central region. The weaker central rolls of $\mathbf{u_d}$, shown in Fig. 3b, are also attenuated as a consequence of the opposition control on v_d. The resulting reduction of $u_d v_d$ explains the slightly flattened $\langle c_f^d \rangle_x$ curve in the central region. In the ROC case, the negative peak of $\langle c_f^{\mathcal{C}} \rangle_x$ is also diminished by more than 30% with respect to the rings-only case. This explains why the drag at the ring sides is higher than in the rings-only case despite $\langle c_f^d \rangle_x$ and $\langle c_f^t \rangle_x$ being much smaller in the same region. More insight into how $\langle c_f^d \rangle_x$ and $\langle c_f^{\mathcal{C}} \rangle_x$ are affected by the OC is obtained by comparing the graphs 12-a (rings-only) and 12-b (ROC case), which show the flow field between two adjacent rings. At the ring sides the core of the negative-u_d region is located further away from the wall in the opposition-control case than in the rings-only case. This effect results in stronger gradients of $u_d + U$ at the wall with respect to the rings-only case. The wall-normal velocity v_d is also mitigated because of the direct opposing action of $v_d(y_d)$. This explains the lower peaks of $\langle c_f^{\mathcal{C}} \rangle_x$ because the term $v_d \partial U / \partial y$ is less intense. The magnitude of $u_d v_d$ is also weakened and its minimum pushed away from the wall, resulting in the maximum of $\langle c_f^d \rangle_x$ being reduced.

We now examine the spatial skin-friction budgets of the RHS case from Fig. 11. On the side regions, $\langle c_f^d \rangle_x$ is increased with respect to the rings-only case. The peaks of

$\langle c_f^t \rangle_x$ is reduced, but less than in the ROC case. In the central region the hydrophobic surface delivers a similar reduction of $\langle c_f^t \rangle_x$ as the ROC case, leading to an average 45% drag reduction. The progressively-averaged $\mathcal{R}_{zp}^t$ curve of Fig. 11 (bottom right graph) also gives about an additional 5% reduction of $\langle c_f^t \rangle_x$ with respect to the rings-only case in the central region, similarly the opposition control case. The behaviour of the zero-global-mean, streamwise-averaged terms $\langle c_f^{\mathcal{C}} \rangle_x$ and $\langle c_f^z \rangle_x$, shown in the second row of Fig. 11, remains largely unchanged.

These insights from the modified FIK analysis can help the future development of drag-reduction strategies, especially methods that require localized actuators. If, similar to our ring actuators, localized actuators interact detrimentally to induce additional Reynolds stresses that increase the wall-shear stress, wall-normal actuation confined between the actuators (wall transpiration in our case) is more efficient than streamwise wall-parallel forcing. We have also learned that the additional benefit of the distributed control in the central part of the ring is limited because the shearing drag-reducing action of the rings already operates effectively there.

Summary

This study has examined two novel drag-reduction methods, i.e., the combination of rotating flush-mounted annular actuators and distributed control methods, i.e., opposition control and hydrophobic surfaces. The main conclusions of our work are outlined in the following.

- *Rings-only flow*

  Despite the significant non-uniformity of the annular actuators, the resulting turbulence statistics are quasi-uniform along the streamwise direction. The ring-side streamwise-aligned structures, generated by the radial flow encountering stationary portion of the wall surfaces at the ring edges and interacting with the flow produced by neighbouring rings, carry a large fraction of the turbulent kinetic energy. While the local effect of these structures is to decrease the wall-shear stress in narrow streamwise-stretched bands between rings because of their negative near-wall streamwise velocity, they are responsible for additional negative ring-flow Reynolds stresses, which globally contribute detrimentally to the turbulent drag. The turbulence intensity at the ring side is larger than in the corresponding reference channel case, whereas the flow over the central part of the ring is almost relaminarized by the action of the spanwise triangular wave generated by the rotating rings. In this central region, the Stokes-type steady boundary layer produced by the rotation of the rings is responsible for the drag reduction and its thickness is equal to the optimal one proper of the streamwise-traveling waves of spanwise wall velocity studied by Quadrio and Ricco (2011). The damping of the turbulence in the central region occurs quite uniformly in the stationary ring core. The total influence of the rings on the turbulence intensity is an attenuation as the central low-turbulence region is much wider than the high-turbulence region of the narrow

elongated structures. For the tip ring velocity and the diameter used in our study, the drag reduction produced by the rings is 20%. A spatially-dependent form of the Fukagata-Iwamoto-Kasagi identity has been useful to quantify the drag-altering effects of each term of the Navier-Stokes equation.

- *Combined flow: rings with distributed control*

  The combined control schemes deliver additional drag reduction with respect to the rings-only case: 7.4% in the case of the spinning rings with opposition control and 6.5% for the spinning rings with hydrophobic surface. We have used an idealized model, based on reasonable assumptions, to predict the drag reduction produced by the combined actuations. The prediction is satisfactory and the ideal values are always slightly larger than the actual drag reduction, which renders the idealized value an upper bound. This simple model can be easily generalized to other combined drag-reduction techniques. The ring-Stokes boundary layer over the central ring region is unaffected by the distributed control schemes, which implies that the drag-reduction effect due to the rings is not altered in the combined cases.

  Although the global drag-reduction performance of the two combined cases is similar, it is achieved via two different mechanisms. The modified form of the Fukagata-Iwamoto-Kasagi identity reveals that the attenuation given by the opposition control is more uniform than that of the hydrophobic surface. The rings-opposition control case exceeds the ideal performance in the side regions, weakening the Reynolds stresses carried by the streamwise-elongated structures at the ring sides. In the central region, the beneficial effect of the opposition control is almost negligible because the wall forcing is directly proportional to the near-wall wall-normal fluctuations, which are already strongly damped by the spinning rings. This view is endorsed by the intense attenuation produced by the opposition control in the central-ring region when the rings are not spinning. The rings-hydrophobic control case fares better in the central-ring region than at the ring sides, where the Reynolds stresses associated with the streamwise structures are strengthened by surface hydrophobicity while the turbulent Reynolds stresses are instead less affected by the surface hydrophobicity than in the opposition-control case. In the central-ring region, the hydrophobicity reduces the drag more than the rings-opposition control method and the flow globally benefits from the mean drag-reducing slip velocity. The distributed-control cases with fixed rings matches the ideal prediction very well, indicating that the additional actual losses are rooted in the interactions between the swirling flow and the distributed controls.

Experiments on wall turbulence over spinning discs and rings is certainly needed for validation of the numerical results. Given the highly three-dimensional character of these flows, the pressure-driven channel flow is certainly a preferred option over the free-stream boundary layer flow without a pressure gradient in order to measure the drag reduction by global pressure-drop measurements. The main reason for this choice

is certainly the difficulty of measuring the highly spatially-dependent wall-shear stress through the wall-normal velocity gradient at the wall. Another very important topic of research is the effect of Reynolds number on the amount of drag reduction produced by the rotating rings and on the scaling of the optimum ring forcing parameters, i.e., the diameters defining the rings and the tip ring velocity, which deliver the maximum attenuation of wall-shear stress. It needs to be verified whether the rings, alone or combined with opposition control, can suppress effectively the large super-structures populating the outer part of high Reynolds number flows (Hutchins and Marusic, 2007). Another point of interest is the possible interaction of the ring-side structures, which scale in outer units (Wise and Ricco, 2014), with the super-structures at high Reynolds numbers.

We close our discussion with a short remark on the implementation of active control techniques in industrial scenarios. As amply discussed in Ricco and Hahn (2013), assuming that wall-unit scaling applies at high Reynolds numbers proper of commercial flight conditions, the optimal ring diameter would be of the order of 1mm and the typical period of rotation would be of the order of 0.1ms. These numbers render the practical realization of the rings method (and of any other active drag reduction technique) extremely difficult. Further complications obviously arise if feedback control is considered, even in the simplistic case of opposition control studied herein, because of the enormous database of the order of terabytes to be processed per second. Nevertheless, motivated by the enormous benefits from economical and environmental aspects, we hope that research in turbulent drag reduction will continue to inspire generation of scientists and receive increased attention in order to achieve the ultimate goal of technological implementation in aircraft industry.

Acknowledgements

The authors acknowledge the EPSRC Grant No. EP/L000261/1 and the UK Turbulence Consortium for providing computer time for the simulations. P.O. would like to thank the Department of Mechanical Engineering at the University of Sheffield and the Gordon Franklin Scholarship for funding this work. S.K.A. was funded by Airbus and the Department of Mechanical Engineering at the University of Sheffield. P.R. was partially funded by the H2020 EU "DRAGY" project. We are indebted to the referees for useful comments and we thank Professor Martin Skote for reading a preliminary version of the manuscript and for providing insightful comments. The text in the paper was written by P.O. and P.R.. The numerical routines for the implementation of the combined control methods were written by S.K.A. (Khosh Aghdam, 2016), although those original routines did not enforce the zero-mass-flow-rate condition at the walls in the hydrophobic case and the wall velocity adjustment along the inner circle of the rings. All the data presented herein are the output of novel simulations carried out by P.O..

References

Adrian, R. (2007). Hairpin vortex organization in wall turbulence. *Phys. Fluids*, 19(4):041301.

Aghdam, S. and Ricco, P. (2016). Laminar and turbulent flows over hydrophobic surfaces with shear-dependent slip length. *Phys. Fluids*, 28(3):035109.

Bidkar, R., Leblanc, L., Kulkarni, A., Bahadur, V., Ceccio, S., and Perlin, M. (2014). Skin-friction drag reduction in the turbulent regime using random-textured hydrophobic surfaces. *Phys. Fluids*, 26(8):085108.

Blesbois, O., Chernyshenko, S., Touber, E., and Leschziner, M. (2013). Pattern prediction by linear analysis of turbulent flow with drag reduction by wall oscillation. *J. Fluid Mech.*, 724:607–641.

Choi, C. and Kim, C. (2006). Large slip of aqueous liquid flow over a nanoengineered superhydrophobic surface. *Phys. Rev. Lett.*, 96(066001).

Choi, H., Moin, P., and Kim, J. (1994). Active turbulence control for drag reduction in wall-bounded flows. *J. Fluid Mech.*, 262:75–110.

Choi, K.-S. (2002). Near-wall structure of turbulent boundary layer with spanwise-wall oscillation. *Phys. Fluids*, 14(7):2530–2542.

Chung, Y. and Talha, T. (2011). Effectiveness of active flow control for turbulent skin friction drag reduction. *Phys. Fluids*, 23(2):025102.

Duque-Daza, C., Baig, M., Lockerby, D., Chernyshenko, S., and Davies, C. (2012). Modelling turbulent skin-friction control using linearized Navier-Stokes equations. *J. Fluid Mech.*, 702:403–414.

Fukagata, K., Iwamoto, K., and Kasagi, N. (2002). Contribution of Reynolds stress distribution to the skin friction in wall-bounded flows. *Phys. Fluids*, 14(11):73–76.

Ge, Z., Holmgren, H., Kronbichler, M., Brandt, L., and Kreiss, G. (2018). Effective slip over partially filled microcavities and its possible failure. *Phys. Rev. Fluids*, 3(5):054201.

Hammond, E., Bewley, T., and Moin, P. (1998). Observed mechanisms for turbulence attenuation and enhancement in opposition-controlled wall-bounded flows. *Phys. Fluids*, 10(9):2421–2423.

Hurst, E., Yang, Q., and Chung, Y. (2014). The effect of Reynolds number on turbulent drag reduction by streamwise travelling waves. *J. Fluid Mech.*, 759:28–55.

Hutchins, N. and Marusic, I. (2007). Evidence of very long meandering features in the logarithmic region of turbulent boundary layers. *J. Fluid Mech.*, 579:1–28.

Jeong, J. and Hussain, F. (1995). On the identification of a vortex. *J. Fluid Mech.*, 285:69–94.

Jung, W., Mangiavacchi, N., and Akhavan, R. (1992). Suppression of turbulence in wall-bounded flows by high-frequency spanwise oscillations. *Phys. Fluids A*, 4(8):1605–1607.

Keefe, L. (1997). A normal vorticity actuator for near-wall modification of turbulent shear flows. *AIAA Paper*, 97-0547.

Keefe, L. (1998). Method and apparatus for reducing the drag of flows over surfaces. *United States Patent*, 5,803,409.

Khosh Aghdam, S. (2016). *Turbulent drag reduction through wall-forcing methods.* PhD thesis, Department of Mechanical Engineering, University of Sheffield.

Laizet, S. and Lamballais, E. (2009). High-order compact schemes for incompressible flows: A simple and efficient method with quasi-spectral accuracy. *J. Comp. Phys.*, 228:5989–6015.

Laizet, S. and Li, N. (2011). Incompact3d: A powerful tool to tackle turbulence problems with up to $\mathcal{O}(10^5)$ computational cores. *Int. J. Num. Meth. Fluids*, 67:1735–1757.

Lardeau, S. and Leschziner, M. (2013). The streamwise drag-reduction response of a boundary layer subjected to a sudden imposition of transverse oscillatory wall motion. *Phys. Fluids*, 25:075109.

Lauga, E. and Stone, H. (2003). Effective slip in pressure-driven Stokes flow. *J. Fluid Mech.*, 489:55–77.

Ling, H., Katz, J., Fu, M., and Hultmark, M. (2017). Effect of Reynolds number and saturation level on gas diffusion in and out of a superhydrophobic surface. *Phys. Rev. Fluids*, 2(12):124005.

Min, T. and Kim, J. (2004). Effects of hydrophobic surface on skin-friction drag. *Phys. Fluids*, 16(7):L55–L58.

Oliver, T., Malaya, N., Ulerich, R., and Moser, R. (2014). Estimating uncertainties in statistics computed from direct numerical simulation. *Phys. Fluids*, 26(3):035101.

Orlandi, P. (2012). *Fluid flow phenomena: a numerical toolkit.* Springer Science & Business Media.

Quadrio, M. (2011). Drag reduction in turbulent boundary layers by in-plane wall motion. *Phil. Trans. Royal Soc. A*, 369(1940):1428–1442.

Quadrio, M. and Ricco, P. (2004). Critical assessment of turbulent drag reduction through spanwise wall oscillations. *J. Fluid Mech.*, 521:251–271.

Quadrio, M. and Ricco, P. (2011). The laminar generalized Stokes layer and turbulent drag reduction. *J. Fluid Mech.*, 667:135–157.

Quadrio, M., Ricco, P., and Viotti, C. (2009). Streamwise-travelling waves of spanwise wall velocity for turbulent drag reduction. *J. Fluid Mech.*, 627:161–178.

Reholon, D. and Ghaemi, S. (2018). Plastron morphology and drag of a superhydrophobic surface in turbulent regime. *Phys. Rev. Fluids*, 3(10):104003.

Reynolds, W. and Hussain, A. (1972). The mechanics of an organized wave in turbulent shear flow. Part 3. Theoretical models and comparisons with experiments. *J. Fluid Mech.*, 54(2):263–288.

Ricco, P. (2004). Modification of near-wall turbulence due to spanwise wall oscillations. *J. Turbul.*, 5 024.

Ricco, P. and Hahn, S. (2013). Turbulent drag reduction through rotating discs. *J. Fluid Mech.*, 722:267–290.

Ricco, P., Ottonelli, C., Hasegawa, Y., and Quadrio, M. (2012). Changes in turbulent dissipation in a channel flow with oscillating walls. *J. Fluid Mech.*, 700:77–104.

Seo, J., García-Mayoral, R., and Mani, A. (2018). Turbulent flows over superhydrophobic surfaces: flow-induced capillary waves, and robustness of air–water interfaces. *J. Fluid Mech.*, 835:45–85.

Skote, M. (2011). Turbulent boundary layer flow subject to streamwise oscillation of spanwise wall-velocity. *Phys. Fluids*, 23:081703.

Viotti, C., Quadrio, M., and Luchini, P. (2009). Streamwise oscillation of spanwise velocity at the wall of a channel for turbulent drag reduction. *Phys. Fluids*, 21(11).

von Kármán, T. (1921). Über laminare und turbulente reibung. *ZAMM J. Appl. Math. and Mechanics/Zeitschrift für Angewandte Mathematik und Mechanik*, 1(4):233–252.

von Storch, H. and Zwiers, F. (2001). *Statistical Analysis in Climate Research*. Cambridge Univ Press.

Wise, D., Alvarenga, C., and Ricco, P. (2014). Spinning out of control: Wall turbulence over rotating discs. *Phys. Fluids*, 26(12):125107.

Wise, D., Olivucci, P., and Ricco, P. (2018). Turbulent drag reduction through oscillating discs–corrigendum. *J. Fluid Mech.*, 856:1064–1066.

Wise, D. and Ricco, P. (2014). Turbulent drag reduction through oscillating discs. *J. Fluid Mech.*, 746:536–564.

Wong, T.-S., Kang, S., Tang, S., Smythe, E., Hatton, B., Grinthal, A., and Aizenberg, J. (2011). Bioinspired self-repairing slippery surfaces with pressure-stable omniphobicity. *Nature*, 477(7365):443–447.

Governing equations for the three-component decomposed flow

We herein summarize the derivation of the governing equations obtained upon the three-dimensional flow decomposition (2.9)-(2.11), following the procedure of Reynolds and Hussain (1972). Substituting (2.9)-(2.11) in the Navier-Stokes equations and applying the time- and symmetry-averaging operators in §2.2 leads to the equation for the i-th component of the average flow $\mathbf{U} + \mathbf{u_d}$:

$$U^j \frac{\partial}{\partial x_s^j}(U^i + u_d^i) + U^j \frac{\partial u_d^i}{\partial x_s^j} = -\frac{\partial p_d}{\partial x_s^i} + \frac{\partial^2}{\partial x_s^j \partial x_s^j}(U^i + u_d^i) - \frac{\partial}{\partial x_s^j}\left(u_d^i u_d^j + \left[\overline{u_t^i u_t^j}\right]_s\right) + \frac{\mathrm{d}P}{\mathrm{d}x_s^i}, \quad \text{(A.1)}$$

where the Einstein repeated-index summation convention is used. The streamwise momentum equation (A.1) reads:

$$\begin{aligned} U\frac{\partial u_d}{\partial x_s} + v_d\frac{\partial U}{\partial y} = &-\frac{\partial p_d}{\partial x_s} + \frac{\partial^2}{\partial x_s^j \partial x_s^j}(U + u_d) - \frac{\partial}{\partial y}(u_d v_d + [\overline{u_t v_t}]_s) \\ &- \frac{\partial}{\partial z_s}(u_d w_d + [\overline{u_t w_t}]_s) - \frac{\partial}{\partial x_s}\left(\left[\overline{u_d^2}\right]_s + \left[\overline{u_t^2}\right]_s\right) + \frac{\mathrm{d}P}{\mathrm{d}x_s}. \end{aligned} \quad \text{(A.2)}$$

The spatial average of (A.2) leads to the equation for the globally-averaged flow:

$$\frac{\partial^2 U}{\partial y^2} - \frac{\partial}{\partial y}(\langle u_d v_d \rangle + [u_t v_t]_g) + \frac{\mathrm{d}P}{\mathrm{d}x_s} = 0. \quad \text{(A.3)}$$

The governing equations for u_d are derived by subtracting (A.3) from (A.1).